Monthly Notices
of the
ROYAL ASTRONOMICAL SOCIETY

MNRAS **453,** 561–580 (2015) doi:10.1093/mnras/stv1660

How well can charge transfer inefficiency be corrected? A parameter sensitivity study for iterative correction

Holger Israel,[1,2⋆] Richard Massey,[1,3] Thibaut Prod'homme,[4] Mark Cropper,[5] Oliver Cordes,[6] Jason Gow,[7] Ralf Kohley,[8] Ole Marggraf,[6] Sami Niemi,[5] Jason Rhodes,[9] Alex Short[4] and Peter Verhoeve[4]

[1]*Institute for Computational Cosmology, Durham University, South Road, Durham DH1 3LE, UK*
[2]*Centre for Extragalactic Astronomy, Durham University, South Road, Durham DH1 3LE, UK*
[3]*Centre for Advanced Instrumentation, Durham University, South Road, Durham DH1 3LE, UK*
[4]*European Space Agency, ESTEC, Keplerlaan 1, NL-2200AG Noordwijk, the Netherlands*
[5]*Mullard Space Science Laboratory, University College London, Holmbury St Mary, Dorking, Surrey RH5 6NT, UK*
[6]*Argelander-Institut für Astronomie, Universität Bonn, Auf dem Hügel 71, D-53121 Bonn, Germany*
[7]*e2v Centre for Electronic Imaging, The Open University, Walton Hall, Milton Keynes MK7 6AA, UK*
[8]*European Space Agency, ESAC, PO Box 78, E-28691 Villanueva de la Cañada, Madrid, Spain*
[9]*Jet Propulsion Laboratory, California Institute of Technology, 4800 Oak Grove Drive, Pasadena, CA 91109, USA*

Accepted 2015 July 20. Received 2015 July 17; in original form 2015 June 25

ABSTRACT

Radiation damage to space-based charge-coupled device detectors creates defects which result in an increasing charge transfer inefficiency (CTI) that causes spurious image trailing. Most of the trailing can be corrected during post-processing, by modelling the charge trapping and moving electrons back to where they belong. However, such correction is not perfect – and damage is continuing to accumulate in orbit. To aid future development, we quantify the limitations of current approaches, and determine where imperfect knowledge of model parameters most degrades measurements of photometry and morphology. As a concrete application, we simulate 1.5×10^9 'worst-case' galaxy and 1.5×10^8 star images to test the performance of the *Euclid* visual instrument detectors. There are two separable challenges. If the model used to correct CTI is perfectly the same as that used to add CTI, 99.68 per cent of spurious ellipticity is corrected in our setup. This is because readout noise is not subject to CTI, but gets overcorrected during correction. Secondly, if we assume the first issue to be solved, knowledge of the charge trap density within $\Delta\rho/\rho = (0.0272 \pm 0.0005)$ per cent and the characteristic release time of the dominant species to be known within $\Delta\tau/\tau = (0.0400 \pm 0.0004)$ per cent will be required. This work presents the next level of definition of in-orbit CTI calibration procedures for *Euclid*.

Key words: instrumentation: detectors – methods: data analysis – space vehicles: instruments.

1 INTRODUCTION

The harsh radiation environment above the Earth's atmosphere gradually degrades all electronic equipment, including the sensitive charge-coupled device (CCD) imaging detectors used in the *Hubble Space Telescope* (*HST*) and *Gaia* (Lindegren et al. 2008), and proposed for use by *Euclid* (Laureijs et al. 2011). While *HST* in its low Earth orbit is exposed primarily to trapped particles held within the Earth's magnetic field, energetic solar and Galactic protons hit *Gaia* at L2, where *Euclid* will orbit (Stassinopoulos & Raymond 1988; Seabroke, Holland & Cropper 2008; Kohley et al. 2014). CCD detectors work by collecting photoelectrons which are stored within a pixel created by an electrostatic potential well. After each exposure, these electrons are transferred via a process called clocking, where alternate electrodes are held high and low to move charge through the pixels towards the serial register. The serial register is then clocked towards the output circuit where charge-to-voltage conversion occurs providing an output signal depending on the charge contained within a pixel. The amount of charge lost with each transfer is described by the charge transfer inefficiency (CTI). One of the results of radiation-induced defects within the silicon lattice is the creation of charge traps at different energy levels within the silicon band-gap. These traps can temporarily capture electrons and release them after a characteristic delay, increasing the CTI. Any electrons captured during charge transfer can re-join

⋆ E-mail: holger.israel@durham.ac.uk

a charge packet later, as spurious charge, often observed as a charge tail behind each source.

Charge trailing can be (partially) removed during image post-processing. Since charge transfer is the last process to happen during data acquisition, the fastest and most successful attempts to correct CTI take place as the second step of data reduction, right after the analogue-to-digital converter bias has been subtracted (e.g. Bristow 2003). By modelling the solid-state physics of the readout process in *HST*'s Advanced Camera for Surveys (ACS), then iteratively reversing the model, Massey et al. (2010) demonstrated a 10-fold reduction in the level of charge trailing. The algorithm was sped up by Anderson & Bedin (2010) and incorporated into the Space Telescope Science Institute default analysis pipeline for HST/ACS (Smith et al. 2012). As the radiation damage accumulated, the trailing got bigger and easier to measure. With an updated and more accurate *HST* model, Massey (2010) achieved a 20-fold reduction. In an independent programme for *Gaia*, Short et al. (2013) developed a model using different underlying assumptions about the solid-state physics in CCDs. Massey et al. (2014) created a meta-algorithm that could reproduce either approach through a choice of parameters, and optimized these parameters for *HST* to correct 98 per cent of the charge trailing.

The current level of achievable correction is acceptable for most immediate applications. However, radiation damage is constantly accumulating in *HST* and *Gaia*, and increasing accuracy is required as data sets grow, and statistical uncertainties shrink. One particularly challenging example of stringent requirements in future surveys will be the measurement of faint galaxy shapes by *Euclid*.

In this paper, we investigate the effect of imperfect CTI correction on artificial images with known properties. We add charge trailing to simulated data using a CTI model $\boldsymbol{M}$, then correct the data using a CTI model with imperfectly known parameters, $\boldsymbol{M} + \delta\boldsymbol{M}$. After each stage, we compare the measured photometry (flux) and morphology (size and shape) of astronomical sources to their true (or perfectly corrected) values. We develop a general model to predict these errors based on the errors in CTI model parameters. We focus on the most important parameters of a 'volume-driven' CTI model: the density ρ_i of charge traps, the characteristic time τ_i in which they release captured electrons, and the power-law index β describing how an electron cloud fills up the physical pixel volume.

This paper is organized as follows. In Section 2, we simulate *Euclid* images and present our analysis methods. In Section 3, we address the challenge of measuring an average ellipticity in the presence of strong noise. We present our CTI model and measure the CTI effects as a function of trap release time-scale τ in Section 4. Based on laboratory measurements of an irradiated CCD273 (Endicott et al. 2012), we adopt a baseline trap model $\boldsymbol{M}$ for the *Euclid* VIS instrument (Section 5). In this context, we discuss how well charge trailing can be removed in the presence of readout noise. We go on to present our results for the modified correction model ($\boldsymbol{M} + \delta\boldsymbol{M}$) and derive tolerances in terms of the trap parameters based on *Euclid* requirements. We discuss these results in Section 6 and conclude in Section 7.

2 SIMULATIONS AND DATA ANALYSIS

2.1 Simulated galaxy images

CTI has the greatest impact on small, faint objects that are far from the readout register (i.e. that have undergone a great number of transfers). To quantify the worst-case scenario, we therefore simulate the smallest, faintest galaxy whose properties are likely to be measured – with an exponential flux profile $f(r) \propto \mathrm{e}^{-r}$ whose broad wings (compared to a Gaussian or de Vaucouleurs profile) also make it more susceptible to CTI. To beat down shot noise, we simulate 10^7 noisy image realizations for each measurement. We locate these galaxies at the far end (Gow et al. 2012, fig. 4), 2051 ± 0.5 pixels from the readout register, and uniformly randomize the sub-pixel centre to average out effects that depend on proximity to a pixel boundary. All our simulated galaxies have the same circularly symmetric profile, following the observation by Rhodes et al. (2010) that this produces the same mean result as randomly oriented elliptical galaxies with no preferred direction.

The visual (VIS) imager, together with the Near Infrared Spectrometer and Photometer, will perform the *Euclid* cosmic shear and galaxy clustering surveys. VIS will deliver deep broad-band optical (550–900 nm) imaging of galaxies with 10σ detection significance for $V = 24.5$ sources, over the whole 15 000 deg^2 extragalactic sky (Cropper et al. 2014). VIS will consist of a 6 × 6 array of e2v CCD273 chips. Each CCD273, in turn, is composed of four sections comprising 2066 × 2048 square pixels of 12 μm, which feed into one readout and amplifier unit. A point spread function (PSF) that is well known and stable in time and over the $\gtrsim 0.5$ deg^2 field of view will secure successful measurement weak lensing down to S/N ≈ 10 galaxies.

Our simulated images are based on VIS simulations in terms of the 0.1 arcsec pixel scale, and preliminary PSF and sky background models, but our setup can easily be adapted to other instruments, e.g. ACS. We create the simulated images spatially oversampled by a factor of 20, convolve them with a similarly oversampled PSF, then resample them to the final pixel scale. To the image signal of ∼1300 electrons, we add a uniform sky background of 105 electrons, as expected for a 560 s VIS exposure, and Poisson photon noise to both the source and the background. After clocking and charge trailing (if it is being done; see Section 4.1), we then add additional readout noise, which follows a Gaussian distribution with a root mean square (rms) of 4.5 electrons, the nominal *Euclid* VIS value.

Before CTI, the galaxies have a mean S/N = 11.35 (and S/N ≈ 10 after correction) and full width at half-maximum (FWHM) size of 0.18 arcsec, as measured by SExtractor (Bertin & Arnouts 1996). This size, the same as the PSF, at the small end of the range expected from fig. 4 of Massey et al. (2013) makes our galaxies the most challenging in terms of CTI correction. These images represent the faintest, smallest galaxies the VIS pipeline is required to analyse. Examples of input, degraded, and corrected images are shown in Fig. 1.

Separately, we perform a second suite of simulations, containing 10^6 realizations of a *Euclid* VIS PSF at S/N ≈ 200, typical of the bright stars from which the VIS PSF is going to be modelled (cf. Cropper et al. 2013). The PSF simulations follow the above recipe, but skip the convolution of the PSF with an exponential disc.

2.2 Image analysis

On each of the sets of images (input, degraded, and corrected), we detect the sources using SExtractor. Moments of the brightness distribution and fluxes of the detected objects are measured using an IDL implementation of the RRG (Rhodes, Refregier & Groth 2001) shape measurement method. RRG is more robust than SExtractor for faint images, combining Gaussian-weighted moments of the image $I(\boldsymbol{\theta})$ to measure integrated source flux

$$F \equiv \int W(\boldsymbol{\theta})\, I(\boldsymbol{\theta})\, \mathrm{d}^2\boldsymbol{\theta}, \tag{1}$$

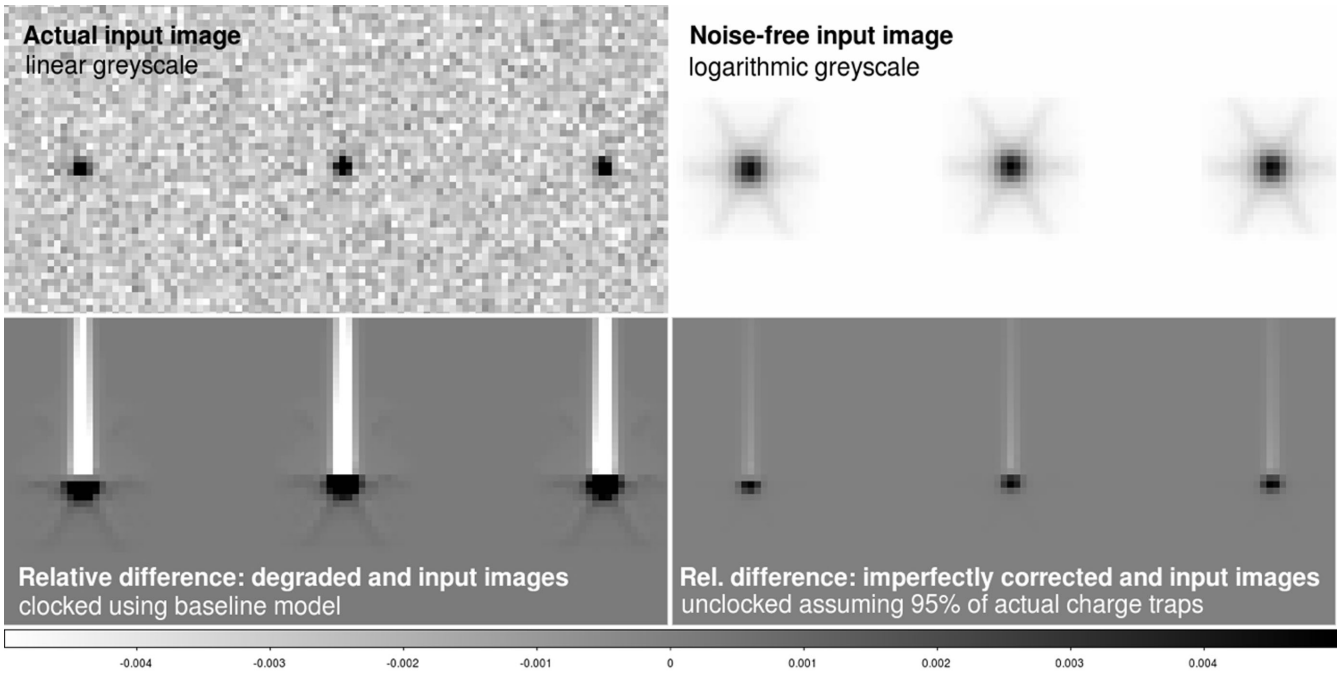

Figure 1. Example of three independent noise realizations of our simulated image of a faint galaxy; each measurement uses 10^7 of these. To the input images (upper-left panel) the clocking is applied, degrading the image by both CTI and readout noise. The lower-left panel shows the relative differences between the degraded and input images for a noise-free realization (upper-right panel). We can correct for the CTI, but not the readout noise (if present), by running the correction software with the trap model as used for clocking. If the correction model deviates from the clocking model, simulating our imperfect knowledge of the trap model, the correction will be imperfect. The lower-right panel shows the relative difference image for a noise-free example, with the same scale as for the degraded image. We explore this imperfection. In noisy images, even the change from input to degraded images is unnoticeable to the naked eye. None the less, a high degree of accuracy in the correction is crucial for *Euclid*'s performance, highlighting its unprecedented sensitivity.

where $W(\boldsymbol{\theta})$ is a Gaussian weight function with standard deviation ω, and the integral extends over 2.5ω; the position

$$y \equiv \int \theta_2\, W(\boldsymbol{\theta})\, I(\boldsymbol{\theta})\, \mathrm{d}^2\boldsymbol{\theta}; \tag{2}$$

the size

$$R^2 \equiv Q_{11} + Q_{22}; \tag{3}$$

and the ellipticity

$$\{e_1, e_2\} \equiv \left\{ \frac{Q_{11} - Q_{22}}{Q_{11} + Q_{22}}, \frac{2Q_{12}}{Q_{11} + Q_{22}} \right\}, \tag{4}$$

where the second-order brightness moments are

$$Q_{\alpha\beta} = \int \theta_\alpha\, \theta_\beta\, W(\boldsymbol{\theta})\, I(\boldsymbol{\theta})\, \mathrm{d}^2\boldsymbol{\theta}, \qquad \{\alpha, \beta\} \in \{1, 2\}. \tag{5}$$

For measurements on stars, we chose a weight function of $\omega = 0.75$ arcsec, the *Euclid* prescription for stars. For galaxies, we seek to reproduce the window functions used in weak lensing surveys. We adopt the radius of the SExtractor object (e.g. Leauthaud et al. 2007) that with $\omega = 0.34$ arcsec truncates more of the noise and thus returns more robust measurements.

Note that we are measuring a raw galaxy ellipticity, a proxy for the (reduced) shear, in which we are actually interested (cf. Kitching et al. 2012, for a recent overview of the effects a cosmic shear measurement pipeline needs to address). A full shear measurement pipeline must also correct ellipticity for convolution by the telescope's PSF and calibrate it via a shear 'responsivity factor' (Kaiser, Squires & Broadhurst 1995). The first operation typically enlarges e by a factor of $\sim$1.6 and the second lowers it by about the same amount. Since this is already within the precision of other concerns, we shall ignore both conversions The absolute calibration of shear measurement with RRG may not be sufficiently accurate to be used in future surveys. However, it certainly has sufficient *relative* accuracy to measure small deviations in galaxy ellipticity when an image is perturbed.

3 HIGH-PRECISION ELLIPTICITY MEASUREMENTS

3.1 Measurements of a non-linear quantity

A fundamental difficulty arises in our attempt to measure galaxy shapes to a very high precision, by averaging over a large number of images. Mathematically, the problem is that calculating ellipticity e_1 directly from the moments and then taking the expectation value $\mathcal{E}(\cdot)$ of all objects, i.e.

$$e_1 = \mathcal{E}\left(\frac{Q_{11} - Q_{22}}{Q_{11} + Q_{22}}\right), \quad e_2 = \mathcal{E}\left(\frac{2Q_{12}}{Q_{11} + Q_{22}}\right), \tag{6}$$

means dividing one noisy quantity by another noisy quantity. Furthermore, the numerator and denominator are highly correlated. If the noise in each follows a Gaussian distribution, and their expectation values are zero, the probability density function of the ratio is a Lorentzian (also known as Cauchy) distribution. If the expectation values of the Gaussians are non-zero, as we expect, the ratio distribution becomes a generalized Lorentzian, called the Marsaglia–Tin distribution (Marsaglia 1965, 2006; Tin 1965). In either case, the ratio distribution has infinite second and first moments, i.e. its variance – and even its expectation value – is undefined. Implications of this for shear measurement are discussed in detail by Melchior &

Viola (2012), Refregier et al. (2012), Kacprzak et al. (2012), Miller et al. (2013), and Viola, Kitching & Joachimi (2014).

Therefore, we cannot simply average over ellipticity measurements for 10^7 simulated images. The mean estimator (equation 6) would not converge, but follow a random walk in which entries from the broad wings of the distribution pull the average up or down by an arbitrarily large amount.

3.2 'Delta-method' (Taylor expansion) estimators for ellipticity

As an alternative estimator, we employ what is called in statistics the 'delta method': a Taylor expansion of equation (6) around the expectation value of the denominator (e.g. Casella & Berger 2002). The expectation value of the ratio of two random variables X, Y is thus approximated by

$$\mathcal{E}(X/Y) \approx \frac{\mathcal{E}(X)}{\mathcal{E}(Y)} - \frac{\mathcal{C}(X,Y)}{\mathcal{E}^2(Y)} + \frac{\mathcal{E}(X)\sigma^2(Y)}{\mathcal{E}^3(Y)} + \frac{\mathcal{C}(X,Y^2)}{\mathcal{E}^3(Y)} - \frac{\mathcal{E}(X)\mathcal{E}[Y-\mathcal{E}(Y)]^3}{\mathcal{E}^4(Y)}, \quad (7)$$

where $\mathcal{E}(X)$, $\sigma(X)$, and $\sigma^2(X)$ denote the expectation value, standard deviation, and variance of X, and $\mathcal{C}(X,Y)$ is its covariance with Y. The zero-order term in equation (7) is the often used approximation $\mathcal{E}(X/Y) \approx \mathcal{E}(X)/\mathcal{E}(Y)$ that switches the ratio of the averages for the average of the ratio. We note that beginning from the first order there are two terms per order with opposite signs. Inserting equation (5) into equation (7), the first-order estimator for the ellipticity reads in terms of the brightness distribution moments $Q_{\alpha\beta}$ as follows:

$$e_1 = \frac{\mathcal{E}(Q_{11}-Q_{22})}{\mathcal{E}(Q_{11}+Q_{22})} - \frac{\sigma^2(Q_{11})-\sigma^2(Q_{22})}{\mathcal{E}^2(Q_{11}+Q_{22})} + \frac{\mathcal{E}(Q_{11}-Q_{22})\sigma^2(Q_{11}+Q_{22})}{\mathcal{E}^3(Q_{11}+Q_{22})} \quad (8)$$

$$e_2 = \frac{\mathcal{E}(2Q_{12})}{\mathcal{E}(Q_{11}+Q_{22})} - \frac{\mathcal{C}(Q_{11},Q_{12})+\mathcal{C}(Q_{12},Q_{22})}{\mathcal{E}^2(Q_{11}+Q_{22})} + \frac{\mathcal{E}(2Q_{12})\sigma^2(Q_{11}+Q_{22})}{\mathcal{E}^3(Q_{11}+Q_{22})}, \quad (9)$$

with the corresponding uncertainties, likewise derived using the delta method (e.g. Casella & Berger 2002):

$$\sigma^2(e_1) = \frac{\sigma^2(Q_{11}-Q_{22})}{\mathcal{E}^2(Q_{11}+Q_{22})} - \frac{\mathcal{E}(Q_{11}-Q_{22})\left[\sigma^2(Q_{11})-\sigma^2(Q_{22})\right]}{\mathcal{E}^3(Q_{11}+Q_{22})} + \frac{\mathcal{E}^2(Q_{11}-Q_{22})\sigma^2(Q_{11}+Q_{22})}{\mathcal{E}^4(Q_{11}+Q_{22})} \quad (10)$$

$$\sigma^2(e_2) = \frac{\sigma^2(Q_{11}+Q_{22})}{\mathcal{E}^2(Q_{11}+Q_{22})} - \frac{\mathcal{E}(Q_{11}+Q_{22})\left[\mathcal{C}(Q_{11},Q_{12})+\mathcal{C}(Q_{12},Q_{22})\right]}{\mathcal{E}^3(Q_{11}+Q_{22})} + \frac{\mathcal{E}^2(Q_{11}+Q_{22})\sigma^2(Q_{11}+Q_{22})}{\mathcal{E}^4(Q_{11}+Q_{22})}. \quad (11)$$

3.3 Application to our simulations

For our input galaxies, the combined effect of the first-order terms in equation (8) is ∼10 per cent. Second-order contributions to the estimator are small, so we truncate after the first order. However, because of the divergent moments of the Marsaglia–Tin distribution, the third- and higher-order contributions to the Taylor series increase again.

Nevertheless, while this delta-method estimator neither mitigates noise bias nor overcomes the infinite moments of the Marsaglia–Tin distribution at a fundamental level, it sufficiently suppresses the random walk behaviour for the purposes of this study, the averaging over noise realizations of the same object. We advocate re-casting the *Euclid* requirements in terms of the *Stokes parameters* ($Q_{11} \pm Q_{22}$, $2Q_{12}$; Viola et al. 2014). These are the numerator and denominator of equation (6) and are well-behaved Gaussians with finite first and second moments.

The formal uncertainties on ellipticity we quote in the rest of this paper are the standard errors $\sigma(e_1)/\sqrt{N}$ given by equation (10). Because our experimental setup re-uses the same simulated sources (computationally expensive due to the large numbers needed), our measurements will be intrinsically correlated (Section 4.2). Hence, the error bars we show overestimate the true uncertainties.

4 THE EFFECTS OF FAST AND SLOW TRAPS

4.1 How CTI is simulated

The input images are degraded using a C implementation of the Massey et al. (2014) CTI model. During each pixel-to-pixel transfer, in a cloud of n_e electrons, the number captured is

$$n_c(n_e) = \exp\left(-\alpha n_e^{1-\beta}\right) \sum_i \rho_i \left(\frac{n_e}{w}\right)^{\beta}, \quad (12)$$

where the sum is over different charge trap species with density ρ_i per pixel and w is the full-well capacity. Parameter α controls the speed at which electrons are captured by traps within the physical volume of the charge cloud, which grows in a way determined by parameter β.

Release of electrons from charge traps is modelled by a simple exponential decay, with a fraction $1 - e^{(-1/\tau_i)}$ escaping during each subsequent transfer. The characteristic release time-scale τ_i depends on the physical nature of the trap species and the operating temperature of the CCD.

In this paper, we make the simplifying 'volume-driven' assumption that charge capture is instantaneous, so $\alpha = 0$. Based on laboratory studies of an irradiated VIS CCD (detailed in Section A), we adopt a $\beta = 0.58$ baseline well fill power and end-of-life total density of one trap per pixel, $\rho = 1$. In our first, general tests, we investigate a single trap species and explore the consequences of different values of τ.

4.2 Iterative CTI correction

The Massey et al. (2014) code can also be used to 'untrail' the CTI. If required, we use $n_{\rm iter} = 5$ iterations to attempt to correct the image (possibly with slightly different model parameters). Note that we perform this correction only after adding readout noise in the simulated images.

Our main interest in this study is the impact of uncertainties in the trap model on the recovered estimate of an observable η (e.g. ellipticity). Therefore, we present our results in terms of differences

between the estimators measured for the corrected images and the input values:

$$\Delta\eta_i = \eta_{i,\mathrm{corrected}} - \eta_{i,\mathrm{input}}. \quad (13)$$

Because for each object of index i the noise in the measurements of $\eta_{i,\,\mathrm{corrected}}$ and $\eta_{i,\,\mathrm{input}}$ are strongly correlated, they partially cancel out. Thus, the actual uncertainty of each $\Delta\eta_i$ is lower than quoted. Moreover, because we re-use the same noise realization in all our measurements (cases of different ρ_i and τ_i), these measurements are correlated as well.

4.3 CTI as a function of trap time-scale

The impact of charge trapping is dependent on the defect responsible. Fig. 2 demonstrates the effect of charge trap species with different release times τ on various scientific observables. To

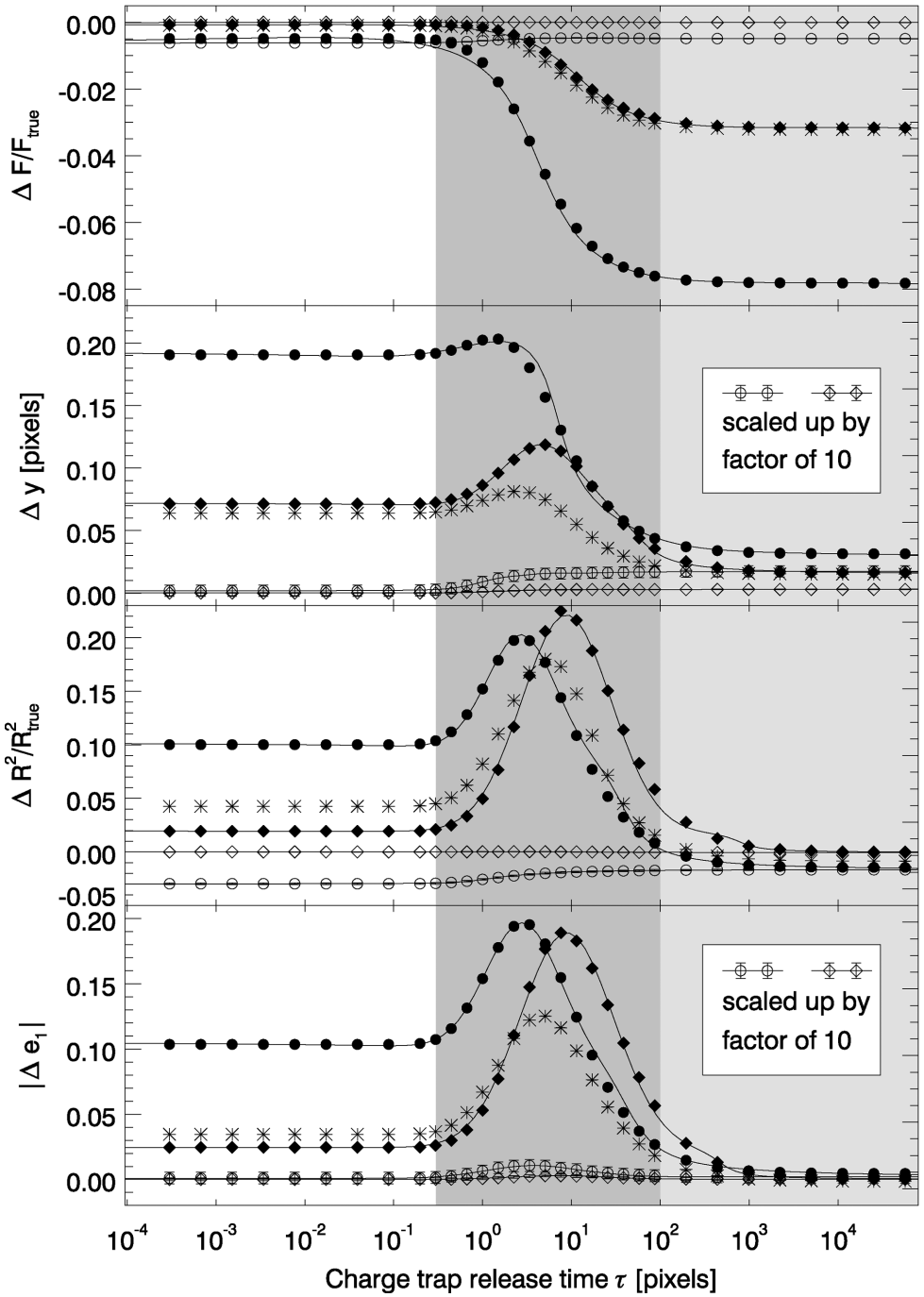

Figure 2. The effect on measurements of galaxy flux F, astrometry y, and morphology (size R^2, ellipticity e_1) of charge traps of different species, i.e. release time-scale τ. The pixel-to-pixel transfer is assumed to be instantaneous. Filled (open) circles denote data for faint galaxies before (after) CTI mitigation, weighted with $\omega = 0.34$ arcsec. Filled (open) diamonds denote data for bright stars before (after) CTI mitigation, weighted with $\omega = 0.75$ arcsec. For comparison, asterisks denote the same stars before mitigation, but weighted with $\omega = 0.34$ arcsec. Area shading marks three different CTI regimes. Lines give the best fit following equation (14), with the coefficients listed in Table 1.

compute each datum, we simulate 10^7 galaxies (filled and open circles), add shot noise, add CTI trailing in the y direction (i.e. vertical in Fig. 1), only then add readout noise. Separately, we simulate 10^6 stars. Using equations (8)–(11), we measure mean values of photometry (top panel), astrometry (second panel), and morphology (size in the third and ellipticity in the bottom panel). Our results confirm what Rhodes et al. (2010) found in a different context.

Three trap regimes are apparent, for all observables highlighted in Fig. 2 by shaded areas. Very fast traps ($\tau \lesssim 0.3$ transfers) do not displace electrons far from the object; thus, their effect on photometry is minimal (top plot in Fig. 2). We observe significant relative changes in position, size, and ellipticity, forming a plateau at low τ, because even if captured electrons are released after the shortest amount of time, some of them will be counted one pixel off their origin. This is probably an artefact. We expect the effect of traps with $\tau < 0.1$ to be different in a model simulating the transfer between the constituent electrodes of the physical pixels, rather than entire pixels.

Very slow traps ($\tau \gtrsim 100$ transfers) result in electrons being carried away over a long distance such that they can no longer be assigned to their original source image. Hence, they cause a charge loss compared to the CTI-free case. However, because charge is removed from nearly everywhere in the image, their impact on astrometry and morphology is small.

The most interesting behaviour is seen in the transitional region, for traps with a characteristic release time of a few transfer times. If electrons re-emerge several pixels from their origin, they are close enough to be still associated with their source image, but yield the strongest distortions in size and ellipticity measurements. This produces local maxima in the lower two panels of Fig. 2. If these measurements are scientifically important, performance can – to some degree – be optimized by adjusting a CCD's clock speed or operating temperature to move release times outside the most critical range $1 \lesssim \tau \lesssim 10$ (Murray et al. 2012).

In the star simulations [filled (open) diamonds in Fig. 2 for degraded (CTI-corrected) images], the CTI effects are generally smaller than for the faint galaxies, because the stars we simulate are brighter and thus experience less trailing *relative to their signal*. The underlying reason is that CTI effects are non-linear and also depend on the filling history: after a strong signal has passed through, long-lived traps will still be filled.

Despite that, we measure about the same spurious ellipticity Δe_1 and even a slightly higher relative size bias $\Delta R^2/R^2_{\rm true}$ for the stars. Partially, this is an artefact due to the larger weight function ($\omega = 0.75$ arcsec for stars, 0.34 arcsec for galaxies). Also, in the right circumstances, the quadratic terms in the second-order moments (equation 5) allow for larger contributions from the outskirts of the object. Notably, the larger ω causes the peak in $\Delta e_1(\tau)$ and $\Delta R^2/R^2_{\rm true}(\tau)$ curves to shift from ~3 pixels for the galaxies to ~9 pixels for the stars. Because the wider window function gives more weight to pixels away from the centroid, the photometry becomes more sensitive to slower traps. Indeed, if we consider the same star images, evaluated with $\omega = 0.34$ arcsec for comparison (asterisks in Fig. 2), the peaks are smaller and located at a smaller τ compared to the default $\omega = 0.75$ arcsec case (filled diamonds). Because the bright stars have more pixels above the background than the faint same-FWHM galaxies, the corresponding peaks are still at larger values of τ, even at the same value of ω.

For a limited number of trap configurations, we have also tried varying the trap density or the number of transfers (i.e. object position on the CCD). In both cases, the dependence is linear. Overall, for all tested observables, the measurements in the degraded images (Fig. 2, solid symbols) are well fitted by the empirical fitting function

$$f^{\rm degrade}(\rho,\tau) = \rho\Big(A + D_{\rm a}\,\mathrm{atan}((\log\tau - D_{\rm p})/D_{\rm w}) + G_{\rm a}\exp\left((\log\tau - G_{\rm p})^2/2G_{\rm w}^2\right)\Big), \quad (14)$$

which combines an arctangent drop ('D') and a Gaussian peak ('G'). The best-fitting amplitudes (A, $D_{\rm a}$ and $G_{\rm a}$), positions on the τ axis ($D_{\rm p}$ and $G_{\rm p}$), and widths ($D_{\rm w}$ and $G_{\rm w}$) are listed in Table 1. The same functional form provides a good match to the residuals after CTI correction, $f^{\rm resid}(\rho,\tau)$ (open symbols in Fig. 2). These residuals are caused by readout noise, which is not subject to CTI trailing, but undergoes CTI correction (see Section 5.3.2).

4.4 Predictive model for imperfect correction

We set out to construct a predictive model $\Delta f^{\rm Pr}$ of $\Delta\eta$, the CTI effect in an observable relative to the underlying true value (equation 13). There are two terms, the CTI degradation (equation 14) and a second term for the effect of the 'inverse' CTI correction allowing for a slightly imperfect CTI model:

$$\Delta f^{\rm Pr} = f^{\rm degr}(\rho,\tau) + f^{\rm correct}(\rho+\Delta\rho,\tau+\Delta\tau). \quad (15)$$

Since CTI trailing perturbs an image by only a small amount, the correction acts on an almost identical image. Assuming the coefficients of equation (14) to be constant, we get

$$\Delta f^{\rm Pr} \approx f^{\rm degr}(\rho,\tau) - f^{\rm degr}(\rho+\Delta\rho,\tau+\Delta\tau) + f^{\rm res}(\rho,\tau), \quad (16)$$

where $f^{\rm res}(\rho,\tau)$ is approximately constant, and depends on the readout noise (see Section 5.3). We could expand this equation as a Taylor series, but the derivatives of f do not provide much further insight.

Because equation (12) is non-linear in the number $n_{\rm e}$ of signal electrons, our observation (Section 4.3) that the *effects* of CTI behave linearly in ρ is not a trivial result. Assuming this linearly in ρ, we can expand equation (16) and factor out ρ. The combined effect of several trap species i with release time-scales τ_i and densities ρ_i can then be written as

$$\Delta f^{\rm Pr}(\rho_i+\Delta\rho_i,\tau_i+\Delta\tau_i) = \sum_i \rho_i f^{\rm resid}(\tau_i) + \sum_i \left[\rho_i f(\tau_i) - (\rho_i+\Delta\rho_i) f(\tau_i+\Delta\tau_i)\right], \quad (17)$$

in which we dropped the superscript of $f^{\rm degr}$ for the sake of legibility. We are going to test this model in the remainder of this study, where we consider a mixture of three trap species. We find equation (17) to correctly describe measurements of spurious ellipticity Δe_1, as well as the relative bias in source size $\Delta R^2/R^2_{\rm true}$ and flux $\Delta F/F_{\rm true}$.

5 *EUCLID* AS A CONCRETE EXAMPLE

5.1 Context for this study

To test the general prediction equation (17), we now evaluate the effect of imperfect CTI correction in simulations of *Euclid* data, with a full *Euclid* CTI model featuring multiple trap species (see Section 5.2). We call this the $\boldsymbol{M} + \delta\boldsymbol{M}$ experiment.

Akin to Prod'homme et al. (2012) for *Gaia*, this study is useful in the larger context of the flow down of requirements from *Euclid*'s science goals (Refregier et al. 2010) to its imaging capabilities

Table 1. Parameters of fitting functions to illustrate the effect on measurements of galaxy fluxes F and F_S, astrometry y and morphology (R^2 and e_1) of charge traps of different species. In all cases, the measurements assume a density of one trap per pixel, and the astrophysical measurement is fitted as a function of the charge trap's characteristic release time τ as $A + D_a \,\mathrm{atan}((\log\tau - D_p)/D_w) + G_a \exp((\log\tau - G_p)^2/2G_w^2)$. Values after correction highlight the efficacy of CTI mitigation.

	A	D_a	D_p	D_w	G_a	G_p	G_w
Galaxy simulation: in degraded images, including readout noise					[10×parameter]		
$\Delta F/F_{true}$	−0.5367 ± 0.0098	−0.3144 ± 0.0085	6.199 ± 0.044	4.639 ± 0.260	0.2116 ± 0.0194	49.53 ± 1.64	41.54 ± 2.39
Δy	1.1098 ± 0.0014	−0.5291 ± 0.0028	8.392 ± 0.080	2.110 ± 0.234	0.3061 ± 0.0185	6.935 ± 0.402	7.083 ± 0.210
$\Delta R^2/R^2_{true}$	0.4226 ± 0.0025	−0.3857 ± 0.0038	15.72 ± 0.18	2.576 ± 0.375	1.0866 ± 0.0448	4.382 ± 0.047	3.779 ± 0.160
Δe_1	0.5333 ± 0.0016	−0.3357 ± 0.0026	16.28 ± 0.22	2.951 ± 0.326	0.9901 ± 0.0203	4.553 ± 0.054	4.132 ± 0.081
Galaxy simulation: after correction in software post-processing (perfect knowledge of charge traps)					[100×parameter]		
$\Delta F/F_{true}$	−0.5549 ± 0.0029	0.0446 ± 0.0028	129.6 ± 13.7	26.00 ± 13.36	0.1301 ± 0.0121	73.47 ± 6.78	56.84 ± 5.21
Δy	0.095 82 ± 0.010 11	0.0517 ± 0.0111	5.622 ± 8.911	2.227 ± 4.557	0.0810 ± 0.1170	2.757 ± 5.369	3.154 ± 2.784
$\Delta R^2/R^2_{true}$	−2.3181 ± 0.0173	0.4431 ± 0.0202	75.90 ± 25.02	28.47 ± 11.03	0.5471 ± 0.2294	41.31 ± 16.09	35.33 ± 9.12
Δe_1	0.013 83 ± 0.0115	0.0039 ± 0.0066	12.30 ± 20.49	1.000 ± 0.000	0.0982 ± 0.0274	5.738 ± 2.085	5.353 ± 2.078
Star simulation: in degraded images, including readout noise					[100×parameter]		
$\Delta F/F_{true}$	−2.2472 ± 0.0239	−1.4558 ± 0.0189	107.5 ± 0.3	55.11 ± 0.95	1.151 ± 0.047	496.6 ± 3.2	343.6 ± 4.4
Δy	4.3532 ± 0.0014	−1.8608 ± 0.0027	173.1 ± 0.4	29.20 ± 0.67	5.0987 ± 0.0173	67.20 ± 0.20	43.91 ± 0.22
$\Delta R^2/R^2_{true}$	0.9489 ± 0.000 98	−6.434 ± 0.0095	288.8 ± 4.7	18.71 ± 4.49	20.237 ± 0.716	94.42 ± 0.15	50.20 ± 0.25
Δe_1	1.2336 ± 0.0077	−0.7941 ± 0.0086	266.7 ± 2.4	17.54 ± 3.90	16.513 ± 0.046	94.87 ± 0.19	52.57 ± 0.21
Star simulation: after correction in software post-processing (perfect knowledge of charge traps)					[100×parameter]		
$\Delta F/F_{true}$	−0.0035 ± 0.0002	0.0027 ± 0.0003	110.2 ± 10.5	42.21 ± 20.02	0.0006 ± 0.0271	182.6 ± 71.3	3.5 ± 100.0
Δy	0.1504 ± 0.000 66	0.0970 ± 0.0067	12.46 ± 1.86	2.731 ± 1.552	0.0218 ± 0.0034	7.377 ± 1.024	5.063 ± 0.717
$\Delta R^2/R^2_{true}$	−0.0163 ± 0.0038	−0.0182 ± 0.0036	1269 ± 33	24.57 ± 47.63	0.0198 ± 0.0146	50.83 ± 34.56	37.95 ± 38.64
Δe_1	0.0012 ± 0.0024	0.0003 ± 0.0014	2.26 ± 50.92	1.000 ± 0.000	0.026 68 ± 0.0061	8.465 ± 1.800	5.379 ± 1.647

(Massey et al. 2013) and instrument implementation (Cropper et al. 2013, 2014). In particular, Massey et al. (2013) highlight that the mission's overall success will be determined both by its absolute instrumental performance and our knowledge about it. We now present the next step in the flow down: to what accuracy do we need to constrain the parameters of the Massey et al. (2014) CTI model? Future work will then determine which calibration observations are required to achieve this accuracy.

While the final *Euclid* requirements remain to be confirmed, we adopt the current values as discussed by Cropper et al. (2013). Foremost, the CTI contribution to the PSF ellipticity shall be $<1.1 \times 10^{-4}$ per ellipticity component.

The *Euclid* VIS PSF model will bear an uncertainty due to CTI, which translates into an additional error on measured galaxy properties. For the bright stars [which have much higher signal-to-noise ratio (S/N)] tracing the PSF, Cropper et al. (2013) quote required knowledge of R^2 to a precision $|\sigma(R^2)| < 4 \times 10^{-4}$. We test this requirement with our second suite of simulations, containing 10^6 realizations of a *Euclid* VIS PSF at S/N ≈ 200 (cf. Section 2.1).

In reality, CTI affects the charge transport in both CCD directions, serial and parallel. For the sake of simplicity, we only consider serial CTI, and thus underestimate the total charge trailing. The total uncertainty in the photometric calibration of VIS science images is required to be <0.7 per cent, with no specific margin allocated to CTI effects.

5.2 CTI model for the *Euclid* VIS instrument

Based on a suite of laboratory test data, we define a baseline model $\boldsymbol{M}$ of the most important CTI parameters (ρ_i, τ_i, β_0). We degrade our set of 10^7 simulated galaxies using $\boldsymbol{M}$. The $\boldsymbol{M} + \delta\boldsymbol{M}$ experiment then consists of correcting the trailing in the degraded images with slight alterations to $\boldsymbol{M}$. We investigate >100 correction models

Table 2. The baseline trap model $\boldsymbol{M}$. The model includes a baseline well fill power of $\beta_0 = 0.58$.

Baseline model	$i = 1$	$i = 2$	$i = 3$
Trap density ρ_i (pixel^{-1})	0.02	0.03	0.95
Release time-scale τ_i (pixel)	0.8	3.5	20.0
Release time-scale τ_i (ms)	186	814	4649

$\boldsymbol{M} + \delta\boldsymbol{M}$, resulting in an impressive 1.4×10^9 simulated galaxies used in this study.

Exposure to the radiation environment in space was simulated in the laboratory by irradiating a prototype of the e2v CCD273 to be used for *Euclid* VIS with a 10 MeV equivalent fluence of 4.8×10^9 protons cm^{-2} (Prod'homme et al. 2014; Verhoeve et al. 2014). Characterization experiments were performed in nominal VIS conditions of 153 K temperature and a 70 kHz readout frequency. We refer to Appendix A for further details on the experiments and data analysis.

We emphasize that our results for e_1 pertain to faint and small galaxies, with an exponential disc profile (see Section 2.1), and placed at the maximum distance from the readout register ($y = 2051$ transfers). Furthermore, we assume the level of radiation damage expected at the end of *Euclid*'s six year mission. Because CTI trailing increases roughly linearly with time in orbit (cf. Massey et al. 2014), the CTI experienced by the typical faintest galaxy (i.e. at half the maximum distance to the readout register and three years into the mission) will be smaller by a factor of 4 compared to the results quoted below.

Where not stated otherwise the nominal *Euclid* VIS rms readout noise of 4.5 electrons was used. Table 2 summarizes the baseline model $\boldsymbol{M}$ that was constructed based on these analyses. The default well fill power is $\beta_0 = 0.58$. Slow traps with $\tau_3 = 20$ clock cycles and $\rho_3 = 0.95$ dominate our baseline model, with small fractions of medium-fast ($\tau_2 = 3.5$, $\rho_2 = 0.03$) and fast ($\tau_1 = 0.8$,

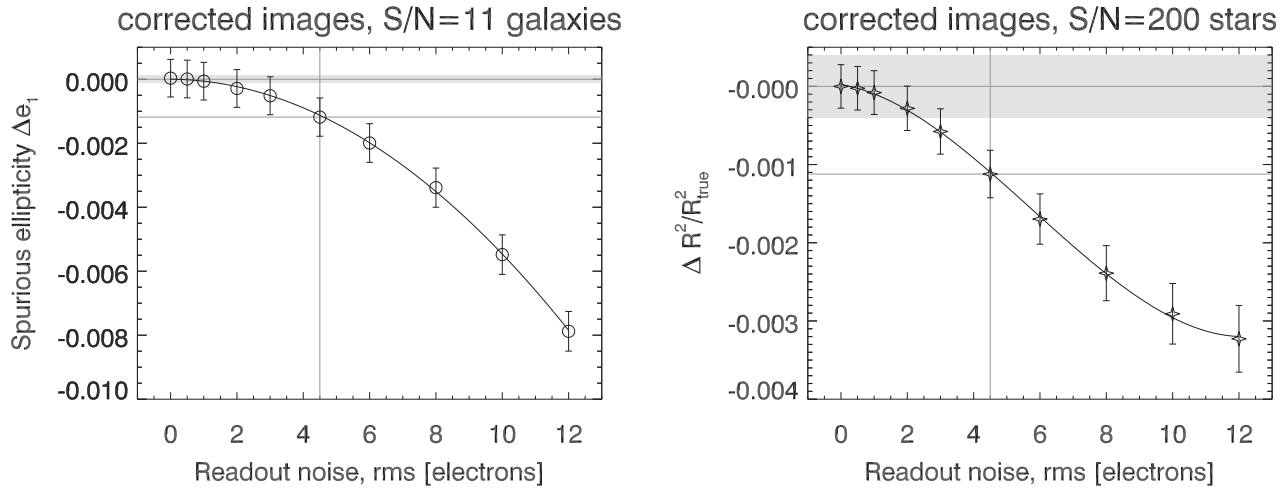

Figure 3. Residual spurious ellipticity and source size induced by CTI after correction, as a function of the rms readout noise. Left plot: spurious ellipticity Δe_1 in the faintest galaxies to be analysed for *Euclid*, at the end of the mission and furthest from the readout register. Right plot: bias in source size $\Delta R^2/R^2_{\rm true}$ in bright stars, at the end of the mission and furthest from the readout register. Lines show the best quadratic (cubic) fits. Shaded regions indicate the *Euclid* VIS requirements. Vertical grey lines mark the nominal rms readout noise of 4.5 electrons.

$\rho_1 = 0.02$) traps. Fig. A3 shows how trails change with changing trap parameters.

5.3 Readout noise impedes perfect CTI correction

5.3.1 Not quite there yet: the zero-point

First, we consider the ellipticities measured in the degraded and corrected images, applying the same baseline model in the degradation and correction steps. The reasons why this experiment does not retrieve the same corrected ellipticity $e_{\rm corr}$ as input ellipticity $e_{\rm in}$ are the Poissonian image noise and Gaussian readout noise. We quantify this in terms of spurious ellipticity $\Delta e = e_{\rm corr} - e_{\rm in}$, and shall refer to it as the *zero-point* of the $\boldsymbol{M} + \delta\boldsymbol{M}$ experiment. The spurious ellipticity in the serial direction is $Z_{e_1} = \Delta e_1 = -0.001\,18 \pm 0.000\,60$. Thus, this experiment on worst-case galaxies using the current software exceeds the *Euclid* requirement of $|\Delta e_\alpha| < 1.1 \times 10^{-4}$ by a factor of $\sim$10. With respect to the degraded image, 99.68 per cent of the CTI-induced ellipticity are being corrected. Virtually the same zero-point, $\Delta e_1 = -0.001\,18 \pm 0.000\,58$, is predicted by adding the contributions of the three species from single-species runs based on the full 10^7 galaxies. We point out that these results on the faintest galaxies furthest from the readout register have been obtained using non-flight readout electronics (cf. Short et al. 2014).

From our simulation of 10^6 bright (S/N $\approx$ 200) stars, we measure the residual bias in source size R^2 after CTI correction of $Z_{R^2} = \Delta R^2/R^2_{\rm true} = (-0.001\,12 \pm 0.000\,30)$, in moderate excess of the requirement $|\Delta R^2/R^2_{\rm true}| < 4 \times 10^{-4}$. We follow Cropper et al. (2013) and Massey et al. (2013) and consider the requirement on CTI, a non-convolutive effect, to pertain to the galaxy images, not to the PSF. However, our data allow us to determine the ellipticity zero-point from our star simulations. We measure $Z^*_{e_1} = \Delta e^*_1 = -0.000\,83 \pm 0.000\,30$. If the $|\Delta e_1| < 1.1 \times 10^{-4}$ requirement were applicable here, it would be missed by $\sim$2/3 of the factor measured for faint galaxies. While the S/N of the star simulations is selected to represent the typical *Euclid* VIS PSF tracers, the same arguments of longest distance from the readout register and non-flight status of the electronics apply.

5.3.2 The effect of readout noise

In Fig. 3, we explore the effect of varying the rms readout noise in our simulations about the nominal value of 4.5 electrons (grey lines) discussed in Section 5.3.1. We continue to use the baseline trap model for both degradation and correction. For the rms readout noise, a range of values between 0 and 15 electrons were assumed. For the faint galaxies (Fig. 3, left plot), we find Δe_1 to increase with readout noise in a way well described by a second-order polynomial. A similar cubic fit can be found for $\Delta R^2/R^2_{\rm true}$ measured from the star simulations (Fig. 3, right plot), but with a hint towards saturation in the highest tested readout noise level.

The most important result from Fig. 3 is that in the absence of readout noise, if the correction assumes the correct trap model $\boldsymbol{M}$, it removes the CTI perfectly, with $\Delta e_1 = (0.3 \pm 5.9) \times 10^{-4}$ and $\Delta R^2/R^2_{\rm true} = (0.0 \pm 2.8) \times 10^{-4}$. The quoted uncertainties are determined by the $N = 10^7$ (10^6) galaxy images we simulated. We conclude that the combination of our simulations and correction code pass this crucial sanity check. If the rms readout noise is $\lesssim$3 electrons ($\lesssim$ 0.5 electrons), the spurious ellipticity (the relative size bias) stays within *Euclid* requirements.

5.4 Sensitivity to imperfect CTI modelling

5.4.1 Morphology biases as a function of well fill power, and determining tolerance ranges

Now that we have assessed the performance of the correction using the same CTI model as for the degradation (given the specifications of our simulations), we turn to the $\boldsymbol{M} + \delta\boldsymbol{M}$ experiment for determining the sensitivities to imperfections in the CTI model. To this end, we assume the zero-point offset Z_{e_1} (or Z_{R^2}) of Section 5.3.1 to be corrected, and 'shift' the requirement range to be centred on it (see, e.g., Fig. 4).

Fig. 4 shows the $\boldsymbol{M} + \delta\boldsymbol{M}$ experiment for the well fill power β. If the degraded images are corrected with the baseline $\beta_0 = 0.58$, we retrieve the zero-point measurement from Section 5.3.1. For the $\boldsymbol{M} + \delta\boldsymbol{M}$ experiment, we corrected the degraded images with slightly different well fill powers $0.56 \leq \beta \leq 0.60$. The upper plot in Fig. 4 shows the resulting Δe_1 in galaxies, and the lower plot

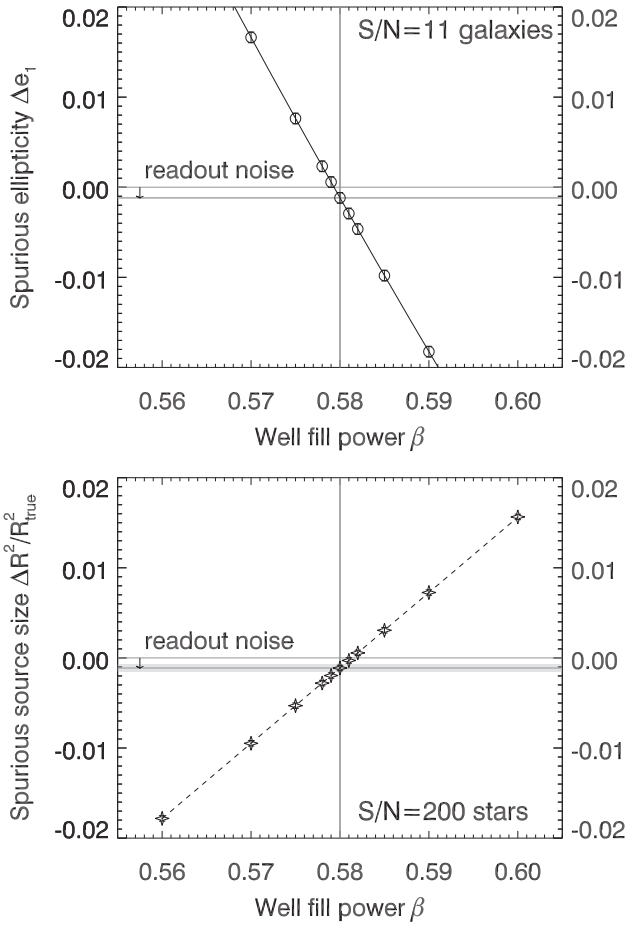

Figure 4. Sensitivity of the CTI-induced spurious ellipticity Δe_1 (upper plot) and the relative spurious source size $\Delta R^2/R^2_{\rm true}$ (lower plot) to the well fill power β. At the default value of $\beta = 0.58$ (vertical grey line), the measurements deviate from zero due to readout noise, as indicated by arrows. The shaded regions around the measurements indicate the *Euclid* requirement ranges as a visual aid. Solid and dashed lines display quadratic (linear) fits to the measured $\Delta e_1(\beta)$ and $\Delta R^2(\beta)/R^2_{\rm true}$, respectively. We study the worst affected objects (at the end of the mission and furthest from the readout register) and the faintest *Euclid* galaxies. This plot also assumes that CTI is calibrated from charge injection lines at full-well capacity only. This will not be the case.

$\Delta R^2/R^2_{\rm true}$ in stars. We find a strong dependence of both the spurious serial ellipticity Δe_1 and $\Delta R^2/R^2_{\rm true}$ on $\Delta\beta = \beta - \beta_0$.

In order to determine a tolerance range with respect to a CTI model parameter ξ with baseline value ξ_0 (here, the well fill power β), we fit the measured bias $\Delta\eta$ (e.g. Δe_1, cf. equation 13) as a function of $\Delta\xi = \xi - \xi_0$. By assuming a polynomial

$$\Delta\eta(\Delta\xi) = Z_\eta + \sum_{j=1}^{J} a_j(\Delta\xi)^j \tag{18}$$

of low order J, we perform a Taylor expansion around ξ_0. In equation 18, Z_η is the zero-point (Section 5.3.1) to which we have shifted our requirement margin. The coefficients a_j are determined using the IDL singular value decomposition least-squares fitting routine `SVDFIT`. For consistency, our fits include Z_η as the zeroth order. In Fig. 4, the best-fitting quadratic (linear) fits to Δe_1 ($\Delta R^2/R^2_{\rm true}$) are shown as a solid and dashed line, respectively.

In both plots, the data stick tightly to the best-fitting lines, given the measurement uncertainties. If the measurements were uncorrelated, this would be a suspiciously orderly trend. However, as already pointed out in Section 3.3, we re-use the same 10^7 simulations with the same peaks and troughs in the noise in all data points shown in Figs 4–9. Hence, we do not expect to see data points to deviate from the regression lines to the degree their quoted uncertainties would indicate. As a consequence, we do not make use of the $\chi^2_{\rm red} \ll 1$ our fits commonly yield for any interpretation.

Because the interpretation of the reduced χ^2 is tainted by the correlation between our data points, we use an alternative criterion to decide the degree J of the polynomial. If the uncertainty returned by `SVDFIT` allows for a coefficient $a_j = 0$, we do not consider this or higher terms. For the panels of Fig. 4, this procedure yields $J = 2$ ($J = 1$). The different signs of the slopes are expected because R^2 appears in the denominator of equation (4).

Given a requirement $\Delta\eta_{\rm req}$, e.g. $\Delta e_{1,\,\rm req} = 1.1 \times 10^{-4}$, the parametric form (equation 18) of the sensitivity curves allows us to derive tolerance ranges to changes in the trap parameters. Assuming the zero-point (the bias at the correct value of ξ) to be accounted for, we find the limits of the tolerance range as the solutions $\Delta\xi_{\rm tol}$ of

$$\left| \sum_{j=1}^{J} a_j(\Delta\xi)^j \right| = \Delta\eta_{\rm req} \tag{19}$$

with the smallest values of $|\Delta\xi|$ on either sides to $\Delta\xi = 0$. Using equation (19), we obtain $\Delta\beta_{\rm tol} = \pm(6.31 \pm 0.07) \times 10^{-5}$ from the requirement on the spurious ellipticity $\Delta e_1 < 1.1 \times 10^{-4}$, for which the quadratic term is small. From the requirement on the relative size bias $\Delta R^2/R^2_{\rm true} < 4 \times 10^{-4}$, we obtain $\Delta\beta_{\rm tol} = \pm(4.78 \pm 0.05) \times 10^{-4}$. In other words, the ellipticity sets the more stringent requirement, and we need to be able to constrain β to an accuracy of at least $(6.31 \pm 0.07) \times 10^{-5}$ in absolute terms. This analysis assumes calibration by a single charge injection line at full-well capacity, such that equation (12) needs to be extrapolated to lower signal levels. We acknowledge that *Euclid* planning has already adopted using also faint charge injection lines, lessening the need to extrapolate.

5.4.2 *Ellipticity bias as a function of trap density*

We now analyse the sensitivity of Δe_α towards changes in the trap densities. Fig. 5 shows the $\boldsymbol{M} + \delta\boldsymbol{M}$ experiment for one or more of the trap densities ρ_i of the baseline model. The upper panel of Fig. 5 presents the spurious ellipticity Δe_1 for five different branches of the experiment. In each of the branches, we modify the densities ρ_i of one or several of the trap species. For example, the upward triangles in Fig. 5 denote that the correction model applied to the images degraded with the baseline model used a density of the fast trap species $\rho_1 + \Delta\rho_1$, tested at several values of $\Delta\rho_1$ with $0.9 \leq 1 + \Delta\rho_1/\rho_1 \leq 1.1$. The densities of the other species are kept to their baseline values in this case. The other four branches modify ρ_2 (downward triangles), ρ_3 (squares), ρ_1 and ρ_2 (diamonds), and all three trap species (circles).

Because a value of $\Delta\rho_i = 0$ reproduces the baseline model in all branches, all of them recover the zero-point measurement of Δe_1 there (cf. Section 5.3.1). Noticing that $e_{\rm degr,\,1} - e_{\rm in,\,1} < 0$ for the degraded images relative to the input images, we explain the more negative Δe_1 for $\Delta\rho_i < 0$ as the effect of undercorrecting the CTI. This applies to all branches of the experiment. Likewise, with increasing $\Delta\rho_i > 0$, the residual undercorrection at the zero-point

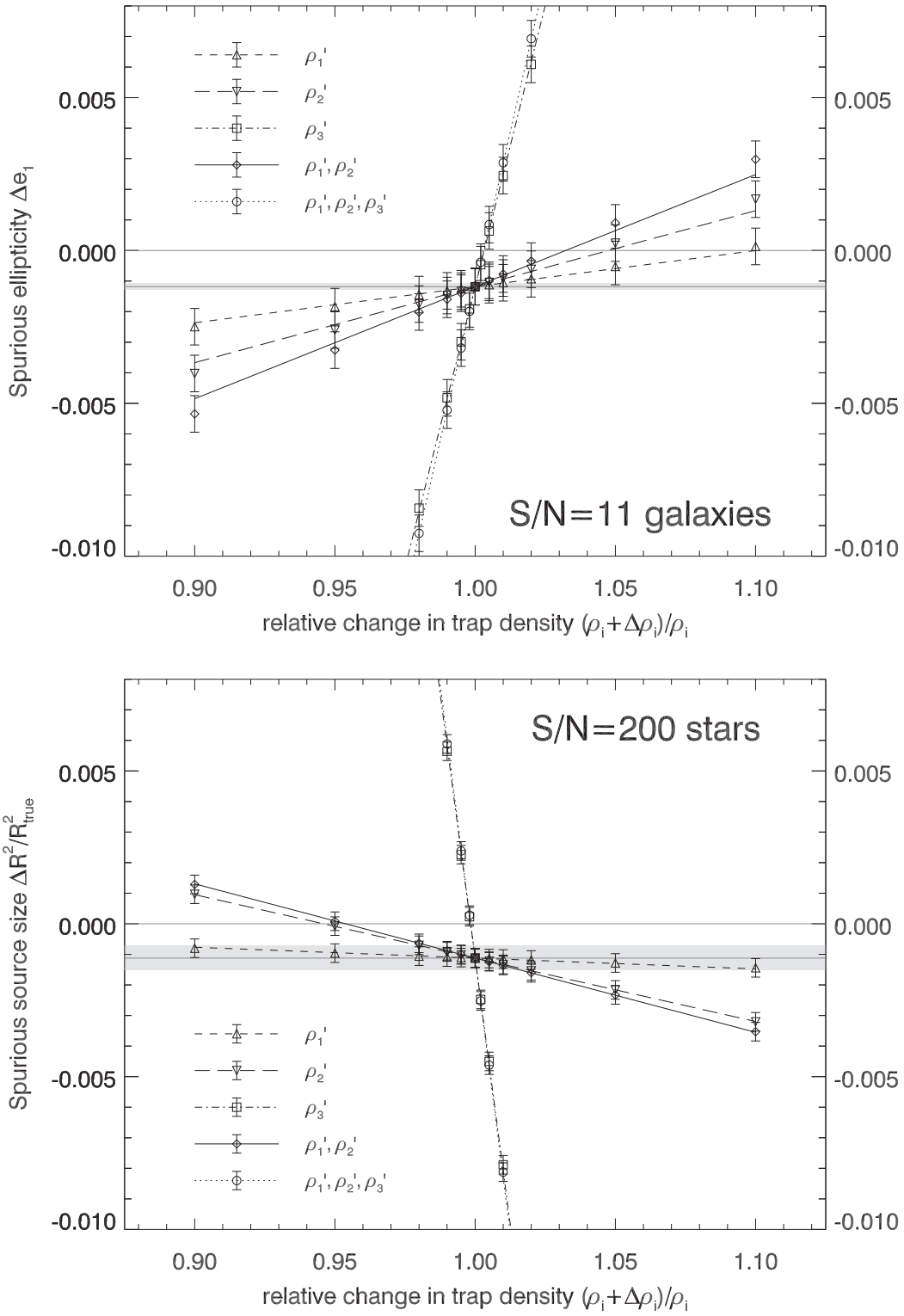

Figure 5. Sensitivity of the CTI-induced spurious ellipticity Δe_1 in faint galaxies (upper panel) and relative bias in source size $\Delta R^2/R^2_{\rm true}$ in bright stars to a relative change in trap densities $(\rho_i + \Delta\rho_i)/\rho_i$. Different symbols and line styles denote to which of the trap species a change in density was applied: the slow traps (ρ_1, upward and dashed line); the medium traps (ρ_2, downward triangles and long-dashed line); both of them (ρ_1, ρ_2, diamonds and triple dot–dashed line); the fast traps (ρ_3, squares and dot–dashed line); all (ρ_1, ρ_2, ρ_3, circles and dotted line). The various broken lines show the best-fitting representation of the measurements as given by the sensitivity model (equation 20). Like in Fig. 4, the grey shaded area indicates the *Euclid* VIS requirement range. We study the worst affected objects (at the end of the mission and furthest from the readout register) and the faintest *Euclid* galaxies.

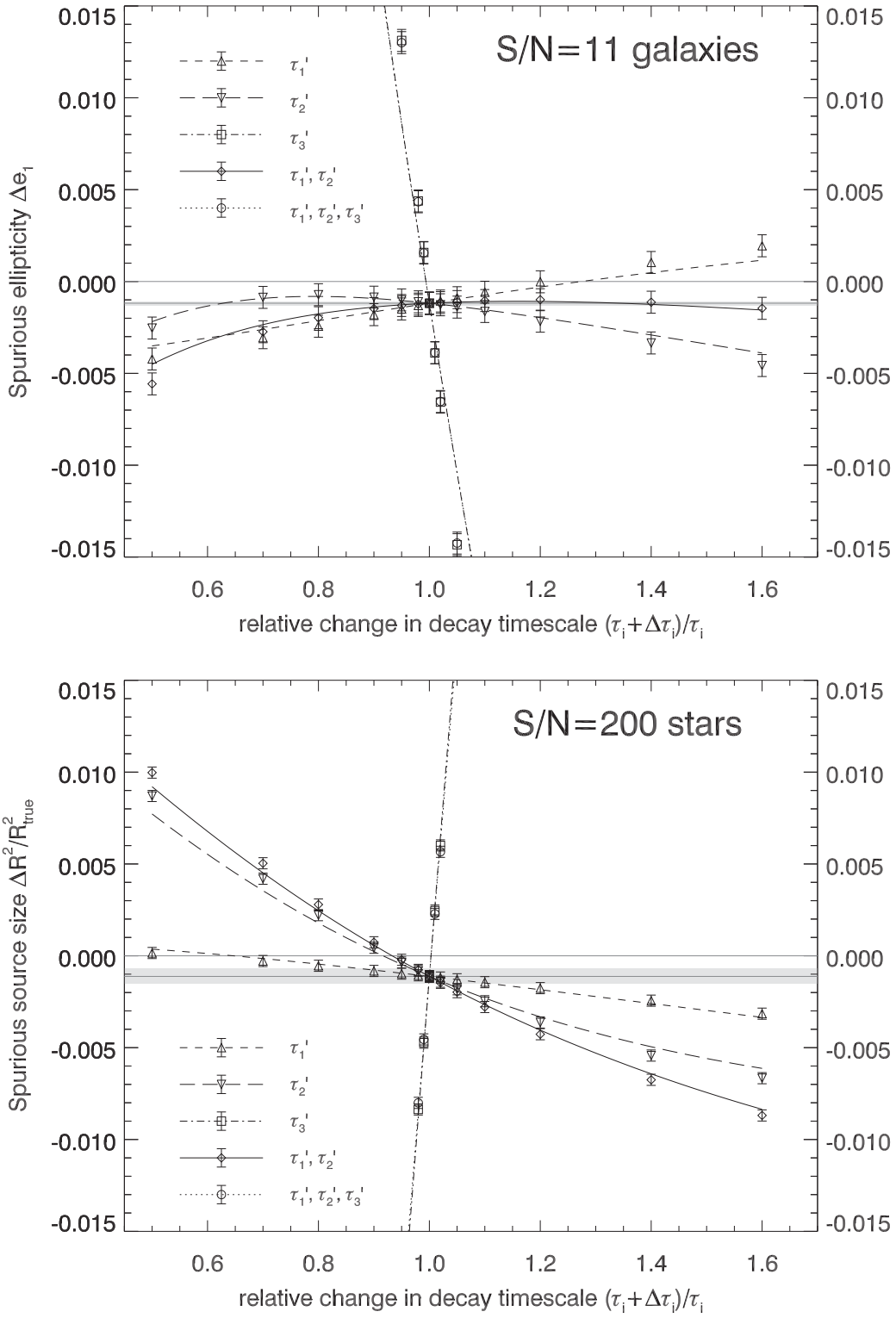

Figure 6. Sensitivity of the CTI-induced spurious ellipticity Δe_1 in faint galaxies (upper panel) and relative bias in source size $\Delta R^2/R^2_{\rm true}$ (lower panel) in bright stars to a relative change in release time-scales $(\tau_i + \Delta\tau_i)/\tau_i$. Different symbols and line styles denote to which of the trap species a change in release time-scale was applied: the slow traps (τ_1, upward triangles and dashed line); the medium traps (τ_2, downward triangles and long-dashed line); both of them (τ_1, τ_2, diamonds and triple dot–dashed line); the fast traps (τ_3, squares and dot–dashed line); all (τ_1, τ_2, τ_3, circles and dotted line). The various broken lines show the best-fitting representation of the measurements as given by the empiric sensitivity model (equation 21). Like in Fig. 4, the grey shaded area indicates the *Euclid* VIS requirement range. We study the worst affected objects (at the end of the mission and furthest from the readout register) and the faintest *Euclid* galaxies.

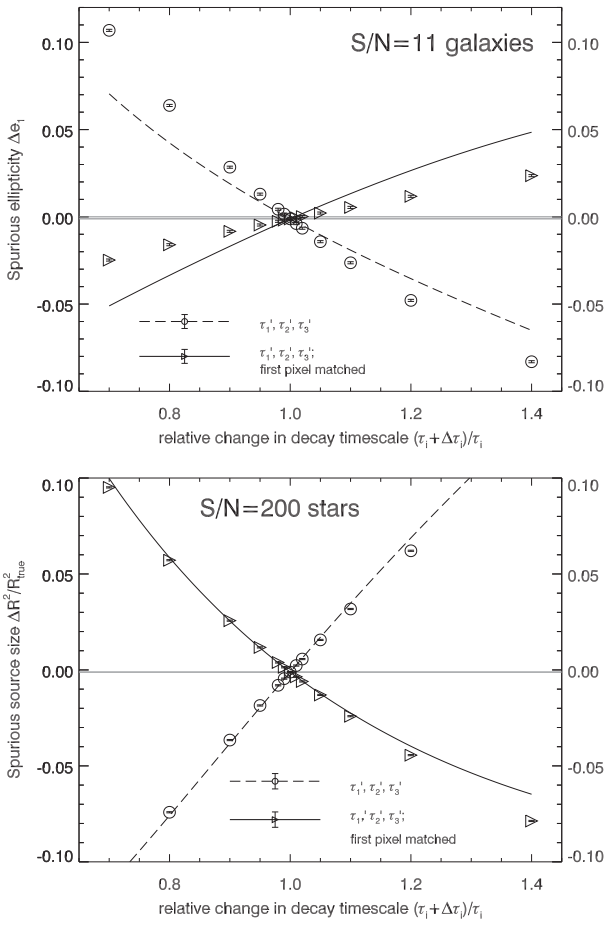

Figure 7. The same as Fig. 6, but for $\Delta\tau_i < 0$ combinations of time-scales τ_i and densities ρ_i that yield the same count rate in the first trail pixel as the baseline model. All trap species are modified in unison (triangles and solid line). For comparison, circles and the dotted line repeat the result from Fig. 6, where only the τ_i were modified, not the ρ_i. (Notice the different scale of the ordinates.) The lines show the predictive models (equation 17). We study the worst affected objects (at the end of the mission and furthest from the readout register) and the faintest *Euclid* galaxies.

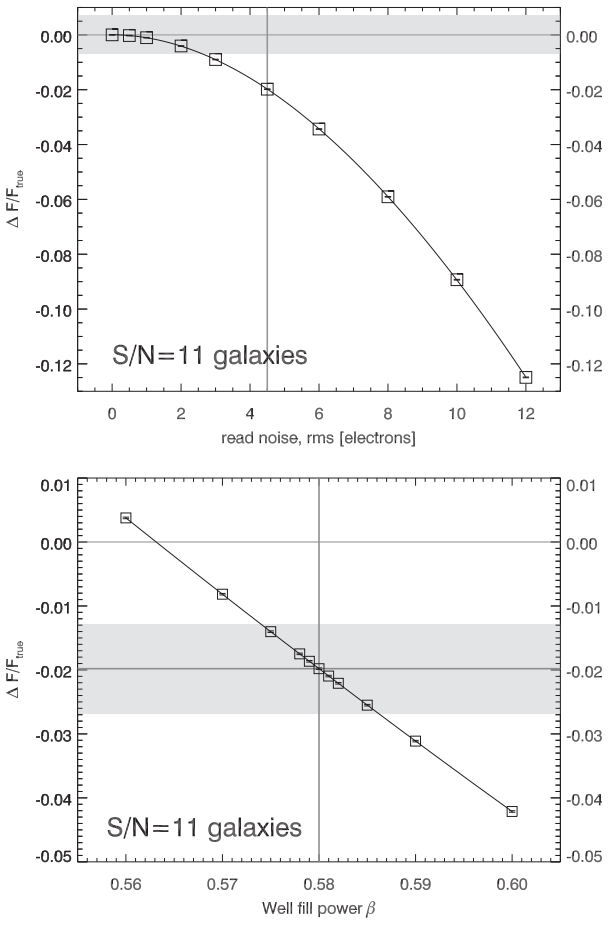

Figure 8. Relative bias in RRG flux with respect to the true input flux, as a function of readout noise (upper panel) and well fill power β (lower panel). Solid lines give the best-fitting polynomial models. The grey shaded *Euclid* requirement range is centred on zero for the readout noise plot and on the zero-point corresponding to the default readout noise for the β plot. Measurement uncertainties are shown, but very small. We study the worst affected objects (at the end of the mission and furthest from the readout register) and the faintest *Euclid* galaxies.

decreases. Eventually, with even higher $\kappa > 1$, we overcorrect the CTI and measure $\Delta e_1 > 0$.

Over the range of $0.9 \leq 1 + \Delta\rho_1/\rho_1 \leq 1.1$ we tested, Δe_1 responds linearly to a change in the densities. Indeed, our model (equation 17), which is linear in the ρ_i and additive in the effects of the different trap species, provides an excellent description of the measured data, both for Δe_1 and $\Delta R^2/R^2_{\rm true}$ (Fig. 5, lower panel). The lines in Fig. 5 denote the model prediction from a simplified version of equation (17),

$$\Delta f^{\rm Pr}(\rho_i + \Delta\rho_i) = \sum_i \rho_i f^{\rm resid}(\tau_i) + \sum_i (\rho_i + \Delta\rho_i) f(\tau_i)\,. \qquad (20)$$

In equation (20), we assumed the τ_i be correct, i.e. $\Delta\tau_i = 0$.

Next, we compute the tolerance $\Delta\rho_{i,\,\rm tol}/\rho$ by which, for each branch of the experiment, we might deviate from the correct trap model and still recover the zero-point within the *Euclid* requirements of $|\Delta e_{\alpha,\,\rm req}| < 1.1 \times 10^{-4}$, resp. $|\Delta R^2_{\rm req}/R^2_{\rm true}| < 4 \times 10^{-4}$. Again, we calculate these tolerances about the zero-points $Z = \sum_i \rho_i f^{\rm resid}(\tau_i)$ (cf. equation 20), which we found to exceed the requirements in Section 5.3.1, but assume to be corrected for in this experiment.

In accordance with the linearity in $\Delta\rho_i$, applying the Taylor expansion recipe of Section 5.4.1, we find the data in Fig. 5 to be well represented by first-order polynomials (equation 18). The results for $\Delta\rho_{i,\,\rm tol}/\rho$ we obtain from equation (19) are summarized in Table 3. For all species, the constraints from Δe_1 for faint galaxies are tighter than the ones from $\Delta R^2/\Delta R^2_{\rm true}$ for bright stars.

Only considering the fast traps, ρ_1 can change by 0.84 ± 0.33 per cent and still be within *Euclid* VIS requirements, given that the measured zero-point has been corrected for. While a tolerance of 0.39 ± 0.06 per cent is found for ρ_2, the slow traps put a much tighter tolerance of 0.0303 ± 0.0007 per cent on the density ρ_3. This is expected because slow traps amount to 95 per cent of all baseline model traps (Table 2). Varying the density of all trap species in unison, we measure a tolerance of 0.0272 ± 0.0005 per cent.

Computing the weighted mean of the $\Delta\tau = 0$ intercepts in Fig. 5, we derive better constraints on the zero-points: $Z_{e_1} = \Delta e_1 = -0.001\,17 \pm 0.000\,08$ for the faint galaxies and $Z_{R^2} = \Delta R^2/R^2_{\rm true} = -0.00\,112 \pm 0.000\,04$ for the bright stars.

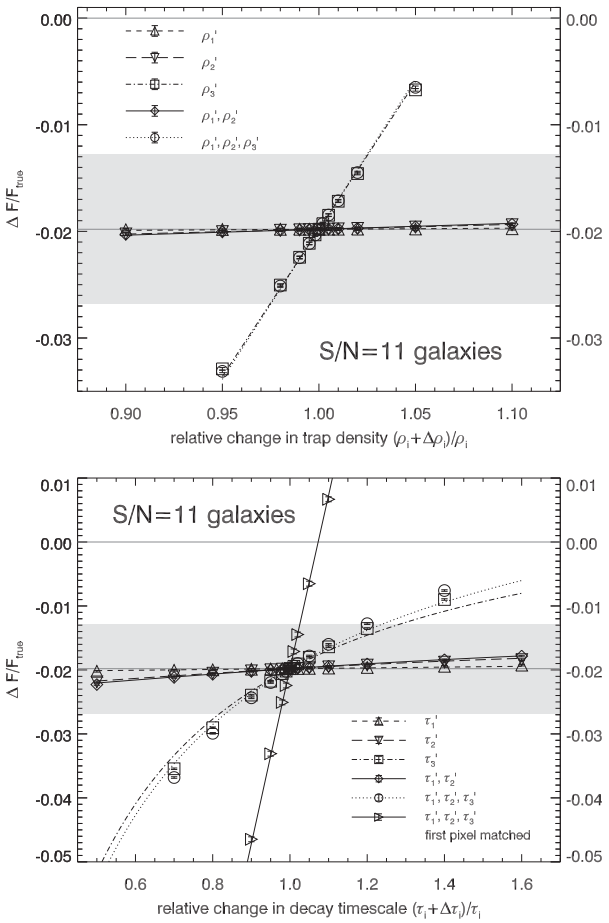

Figure 9. Upper panel: the same as Fig. 5, but showing the sensitivity of the measured flux bias $\Delta F/F_{\rm true}$ as a function of the relative change in trap densities ρ_i. Lower panel: the same as Fig. 6, but showing the flux bias $\Delta F/F_{\rm true}$ as a function of the relative change in trap densities τ_i. Right-pointing triangles and the solid line denote the all-species 'first pixel matched'. The lines in both panels show the predictive model (equation 17). We study the worst affected objects (at the end of the mission and furthest from the readout register) and the faintest *Euclid* galaxies.

5.4.3 *Ellipticity bias as a function of trap release time*

Fig. 6 shows the $\boldsymbol{M}+\delta\boldsymbol{M}$ experiment for one or more of the release time-scales τ_i of the trap model. The upper panel of Fig. 6 presents the spurious ellipticity Δe_1 for five different branches of the experiment. In each of the branches, we modify the release time-scales τ_i of one or several of the trap species by multiplying it with a factor $(\tau_i+\Delta\tau_i)/\tau_i$.

As in Fig. 5, the upward triangles in Fig. 6 denote that the correction model applied to the images degraded with the baseline model used a density of $\tau_1+\Delta\tau_1$ for the fast trap species. The release time-scales of the other species are kept to their baseline values in this case. The other four branches modify τ_2 (downward triangles), τ_3 (squares), τ_1 and τ_2 (diamonds), and all three trap species (circles).

Because a value of $\Delta\tau=0$ reproduces the baseline model in all branches, all of them recover the zero-point measurement of Δe_1 there. The three trap species differ in how the Δe_1 they induce varies as a function of $\Delta\tau_i$. One the one hand, for τ_1, we observe more negative Δe_1 for $(\tau_i+\Delta\tau_i)/\tau_i<1$, and less negative values for $(\tau_i+\Delta\tau_i)/\tau_i>1$, with a null at $(\tau_i+\Delta\tau_i)/\tau_i\approx1.5$. On the other hand, with the slow traps (τ_3), we find $\Delta e_1>0$ for $(\tau_i+\Delta\tau_i)/\tau_i\lesssim0.99$, and more negative values than the zero-point for $(\tau_i+\Delta\tau_i)/\tau_i>1$. The curve of $\Delta e_1(\lambda\tau_2)$ shows a maximum at $(\tau_i+\Delta\tau_i)/\tau_i\approx0.8$, with a weak dependence on $0.7\lesssim(\tau_i+\Delta\tau_i)/\tau_i\lesssim1.1$.

Key to understanding the spurious ellipticity as a function of the τ_i is the dependence of $\Delta e_1(\tau)$ for a single trap species that we presented in Fig. 2, and expressed by the empirical fitting function $f_{{\rm e}_\alpha}(\tau)$ (equation 14) with the parameters quoted in Table 1. While the correction algorithm effectively removes the trailing when the true τ_i is used, the residual of the correction will depend on the difference between the Δe_α for τ_i and for the time-scale $(\tau_i+\Delta\tau_i)/\tau_i$ actually used in the correction. This dependence is captured by the predictive model (equation 17), which simplifies for the situation in Fig. 6 ($\Delta\rho_i=0$) to

$$\Delta f^{\rm Pr}(\tau_i+\Delta\tau_i)=Z+\sum_i\rho_i\,[f(\tau_i)-f(\tau_i+\Delta\tau_i)]\,, \qquad (21)$$

with $Z=\sum_i\rho_i f^{\rm resid}(\tau_i)$ (lines in Fig. 6). In the branches modifying τ_1 and/or τ_2, but not τ_3, the measurements over the whole range of $0.5\leq(\tau_i+\Delta\tau_i)/\tau_i\leq1.6$ agree with the empirical model within their uncertainties. If τ_3 is varied, equation (21) overestimates $|\Delta e_1|$ significantly for $|\Delta\tau_i|>0.05\tau_i$. We discuss a possible explanation in Section 6. Our empirical model provides a natural explanation for the maximum in $\Delta e_1(\tau_2)$. Because $\tau_2=3.5$ is located near the peak in $f_{{\rm e}_1}(\tau)$, assuming $(\tau_i+\Delta\tau_i)/\tau_i\leq0.8$ for correction means using a release time regime where $\Delta e_1(\tau)$ is still rising instead of falling. The correction software accounts for this; hence, the spurious ellipticity from using the wrong release time-scale shows the same maximum as $f_{{\rm e}_1}(\tau)$.

Because τ_2 is not located very closely to the peak in $\Delta R^2/\Delta R^2_{\rm true}(\tau)$ (cf. Fig. 2), we do not see an extremum in the lower panel of Fig. 6 which shows the sensitivity of the size bias in bright stars to variations in the τ_i.

In order to compute the tolerances $\Delta\tau_{\rm tol}$ towards changes in the release time-scales, we again employ a polynomial fit (equation 19). Evidently, the tolerances differ substantially between the τ_i, again with the narrower tolerance intervals from Δe_1 than from $\Delta R^2/\Delta R^2_{\rm true}$. Only for $\Delta\tau_2$ with its extreme point for Δe_1 near the baseline value, we find similar tolerances in both cases. However, even for the rare trap species τ_1, the tolerance is only $\Delta\tau_{1,\,\rm tol}=(1.93\pm0.23)$ per cent. One needs to know the release time-scale of the slow trap species to an accuracy of (0.0400 ± 0.0004) per cent to be able to correct it within *Euclid* VIS requirements. We find the same tolerance if all time-scales are varied in unison.

5.4.4 *Combinations of time-scales and densities yielding the same first trail pixel flux*

Considering how trap parameters are constrained practically from extended pixel edge response (EPER) and first pixel response (FPR) data, it is instructive to consider combinations of trap release time-scales τ_i and densities ρ_i that yield the same number of electrons in the first pixel of the trail as the baseline model. This is interesting because given realistic conditions, the first pixel of the trail will have the largest S/N and will be most easily constrained. We thus perform an initial exploration of the parameter degeneracies. In our 'first pixel matched' models, the effect of a given change in τ on the first trail pixel needs to be compensated by a change in ρ. Because a larger (smaller) τ means more (less) charge close to the original

Table 3. Tolerances for changes in the trap model parameters ξ (column 1), derived from polynomial fits to the sensitivity curves, and taking into account the *Euclid* VIS requirements (equations 18 and 19). Here, we assume no residual biases when using the correct trap model. For three observables η, we show pairs of tolerances, for $\Delta\xi < 0$ and $\Delta\xi > 0$ each. Columns 2 and 3 report tolerances based on the ellipticity bias Δe_1, columns 4 and 5 those from the relative size bias $\Delta R^2/R^2_{\rm true}$, and columns 6 and 7 those from the relative flux bias $\Delta F/F_{\rm true}$. FPM denotes the 'first pixel matched' case for $\tau_{1,2,3}$ and $\rho_{1,2,3}$.

Branch ξ	$10^4\,\Delta\xi^{\rm min}_{\rm tol}$ $\eta=\Delta e_1$ galaxies	$10^4\,\Delta\xi^{\rm max}_{\rm tol}$ $\eta=\Delta e_1$ galaxies	$10^4\,\Delta\xi^{\rm min}_{\rm tol}$ $\eta=\Delta R^2/R^2_{\rm true}$ stars	$10^4\,\Delta\xi^{\rm max}_{\rm tol}$ $\eta=\Delta R^2/R^2_{\rm true}$ stars	$10^4\,\Delta\xi^{\rm min}_{\rm tol}$ $\eta=\Delta F/F_{\rm true}$ galaxies	$10^4\,\Delta\xi^{\rm max}_{\rm tol}$ $\eta=\Delta F/F_{\rm true}$ galaxies
β	-0.631 ± 0.007	0.631 ± 0.007	-4.78 ± 0.05	4.78 ± 0.05	-61.5 ± 0.3	60.5 ± 0.3
ρ_1	-84^{+18}_{-33}	84^{+33}_{-18}	-1250^{+450}_{-1800}	1250^{+1800}_{-450}	–	–
ρ_2	-39^{+4}_{-6}	39^{+6}_{-4}	-191^{+16}_{-19}	191^{+19}_{-16}	–	–
ρ_3	$-3.03^{+0.06}_{-0.07}$	$3.03^{+0.07}_{-0.06}$	-5.91 ± 0.03	5.91 ± 0.03	-267.5 ± 1.6	267.5 ± 1.6
$\rho_{1,2}$	-26^{+2}_{-3}	26^{+3}_{-2}	-166^{+12}_{-14}	166^{+14}_{-12}	–	–
$\rho_{1,2,3}$	-2.72 ± 0.05	2.72 ± 0.05	-5.71 ± 0.03	5.71 ± 0.03	-262.8 ± 1.6	262.8 ± 1.6
τ_1	-193^{+19}_{-23}	193^{+23}_{-19}	-1310^{+120}_{-150}	1310^{+150}_{-120}	$<-10\,000$	$>10\,000$
τ_2	-300^{+90}_{-360}	270^{+150}_{-70}	-270^{+50}_{-70}	270^{+80}_{-50}	$<-10\,000$	$>10\,000$
τ_3	-4.00 ± 0.04	4.00 ± 0.04	-11.30 ± 0.05	11.31 ± 0.05	-1574^{+24}_{-23}	2320^{+100}_{-90}
$\tau_{1,2}$	-420^{+150}_{-420}	700^{+900}_{-400}	-220^{+30}_{-50}	230^{+50}_{-40}	$<-10\,000$	$>10\,000$
$\tau_{1,2,3}$	-4.03 ± 0.04	4.04 ± 0.04	-11.69 ± 0.05	11.68 ± 0.05	-1454^{+19}_{-20}	2020^{+70}_{-60}
$\tau_{1,2,3}$, $\rho_{1,2,3}$, first pixel matched	$-16.07^{+0.57}_{-0.61}$	$16.09^{+0.61}_{-0.57}$	-16.17 ± 0.09	16.21 ± 0.09	-262.5 ± 0.7	263.0 ± 0.7

pixel, the compensation requires $\Delta\rho_i < 0$ for $\Delta\tau_i < 1$ and $\Delta\rho_i > 1$ for $\Delta\tau_i > 1$. Only in the branches where we vary τ_3 or all time-scales together, we find the $\Delta\rho_i$ to differ noticeably from unity. For the latter two, they populate a range between $\Delta\rho_i = 0.745$ for $\Delta\tau_i = 0.7$ and $\Delta\rho_i = 1.333$ for $\Delta\tau = 1.4$.

Fig. 7 shows the $\boldsymbol{M} + \delta\boldsymbol{M}$ experiment for all τ_i and ρ_i (triangles). Circles depict the alteration to τ_i, but with the ρ_i kept fixed, i.e. the same measurement as the circles in Fig. 6. Compared to these, Δe_1 in faint galaxies (upper panel) is of opposite sign in the 'first pixel matched' case, relative to the zero-point. This can be understood as an effect of our baseline trap mix being dominated by slow traps, for which a small increase in τ leads to *less* CTI-induced ellipticity. The simultaneous increase in trap density affects *more* CTI-induced ellipticity, and this is the larger of the two terms, such that a change in sign ensues. The same holds for $\Delta R^2/R^2_{\rm true}$ in bright stars (lower panel of Fig. 7), but with inverted slopes compared to Δe_1.

Again using equation (19), we compute the tolerance range for the changes to the τ_i in the 'first pixel matched' case. (The respective changes to the ρ_i are determined by the first pixel constraint.) Modifying all release time-scales, we arrive at $\Delta\tau_{\rm tol} = 0.16$ per cent (Table 3). This tolerance is wider than the 0.04 per cent for Δe_1 when only the τ_i are varied, again due to the different signs arising from variations to τ_3 and ρ_3. By coincidence, we also arrive at $\Delta\tau_{\rm tol} = 0.16$ per cent when repeating that test with the size bias measured in bright stars.

The black solid line in Fig. 7 shows the predictive model (equation 17), taking into account the combined effect of the $\Delta\tau_i$ and $\Delta\rho_i$, giving the same first pixel flux. Both in the τ_i-only (dotted line) and 'first pixel matched' cases, it matches the measurements only within a few per cent from $(\tau_i + \Delta\tau_i)/\tau_i = 1$. Crucially, this mismatch only occurs for Δe_1 in faint galaxies, but not for $\Delta R^2/R^2_{\rm true}$ in bright stars.

We explain this discrepancy with the uncertainties with which our measurements and modelling (Fig. 2) describe the underlying function $f_{e_1}(\tau)$. The range $20 \lesssim \tau \lesssim 100$ is where the fitting function (equation 14) deviates most from the observations in Fig. 2. The CTI correction effectively removes almost all CTI effects on photometry and morphology, leaving the residuals presented in Figs 5–9, at least one order of magnitude smaller than the scales of the uncorrected CTI effects. Hence, a relatively small uncertainty in $f(\tau)$ causes a large mismatch with the data.

The cause of the uncertainty in the parameters of equation (14), shown in Table 1, is twofold. First, there is uncertainty in the fit as such. Secondly, there is uncertainty due to the finite sampling of the $\Delta e_\alpha(\tau)$ and $\Delta F_{\rm rel}(\tau)$ curves. Running a denser grid in τ can remove the latter, but the former might be ultimately limited by our choice of the function (equation 14), which is empirically motivated, not physically. We further discuss the limits of the predictive model in Section 6.

5.5 Residual flux errors after imperfect CTI correction

5.5.1 Flux bias as a function of readout noise

Given the default rms readout noise of 4.5 electrons, we measure a flux bias $\Delta F_{\rm rel} = \Delta F/F_{\rm true}$ relative to the true flux $F_{\rm true}$ in the input faint galaxy simulations of (-1.980 ± 0.012) per cent after CTI correction, corresponding to 92.9 per cent of the CTI-induced flux bias being corrected. The upper panel of Fig. 8 shows the relative flux biases before and after correction as a function of rms readout noise. Without readout noise, the flux bias can be corrected perfectly ($\Delta F_{\rm rel} = (0.002 \pm 0.012) \times 10^{-2}$ after correction). With increasing readout noise, the flux bias deteriorates, in a way that can be fitted with a cubic polynomial in terms of readout noise. Comparing to the degraded images, we notice that the correction software applies same amount of correction, independent of the readout noise. Because the mitigation algorithm in its current form does not include a readout noise model, this confirms our expectations.

We show the *Euclid* requirement on photometric accuracy as the grey shaded area in Fig. 8 (upper panel), centred on zero. The nominal readout noise case exceeds the requirement of <0.7 per cent photometric uncertainty for the faintest, worst affected galaxies we study. However, the CTI-induced bias affects all VIS images, and would thus be calibrated out. The *Euclid* flux requirement can be understood as pertaining to *uncertainties*, not *biases* in the photometric calibration. The uncertainty of the flux bias, 0.0012 per cent,

then makes only a small contribution to the photometric error budget. We now go on to study the sensitivity of the flux bias towards changes in the trap model.

5.5.2 *Flux bias as a function of well fill power β*

The lower panel of Fig. 8 shows how a change in well fill power β alters the flux bias. If we correct the degraded images using a $\beta > \beta_0$, the model accounts for less CTI in small charge packages, i.e. less CTI in the image's wings that are crucial for both photometry and morphology (cf. Fig. 4). Hence, a $\beta > \beta_0$ leads to an undercorrection relative to the flux bias zero-point Z_F (Section 5.5.1), while for $\beta - \beta_0 \lesssim -0.017$, the zero line is crossed and overcorrection occurs.

Although $\Delta F_\mathrm{rel}(\beta)$ in Fig. 8 appears linear, using the criterion based on significant components (Section 5.4.2), a quadratic is preferred, indicated by the solid line. Using equation (19), we compute the tolerance range in β given $\Delta F_\mathrm{rel}(\beta_\mathrm{tol}) = 0.007$, centred on Z_F. Towards smaller well fill powers, we find $\Delta\beta_\mathrm{tol}^\mathrm{min} = -(6.15 \pm 0.03) \times 10^{-3}$, while towards larger β, we find $\Delta\beta_\mathrm{tol}^\mathrm{max} = (6.05 \pm 0.03) \times 10^{-3}$. Compared to the constraints on the knowledge of β from Δe_1 derived in Section 5.4.1, these margins are $\sim$100 times wider.

5.5.3 *Flux bias as a function of trap densities*

The upper plot of Fig. 9 shows the flux bias ΔF_rel in dependence of a change $\Delta\rho_i$ to the densities ρ_i in the correction model, in analogy with Section 5.4.2. Unless the density of the dominant trap species ρ_3 is modified, we measure only insignificant departures from the zero-point Z_F. Given the high accuracy of the flux measurements, these are still significant measurements, but they are negligible with respect to the *Euclid* requirement on flux. If all ρ_i are varied in unison, the effect on ΔF_rel is largest. A linear model using equation (18) yields a tolerance of $\Delta\rho_i^\mathrm{tol}/\rho_i = \pm 2.628 \pm 0.016$ per cent, wider than the tolerances for Δe_1 or $\Delta R^2/R^2_\mathrm{true}$ (Table 3). The lines in the upper plot of Fig. 9 show that the model (equation 20) matches our measurements well over the range in $\Delta\rho_i$ we tested.

5.5.4 *Flux bias as a function of release time-scales*

The lower plot of Fig. 9 shows the flux bias ΔF_rel in dependence of a change $\Delta\tau_i$ in the correction model, like in Section 5.4.3. As for varying the ρ_i (Section 5.5.3), a change to only the fast and/or the medium traps yields only small departures from the zero-point such that we can bundle together all trap species for deriving a tolerance range. The respective measurements (black circles in Fig. 9) show a steep slope at $\Delta\tau_i < 0$ that flattens out to $\Delta\tau_i > 0$. This can be explained given the saturation of ΔF_rel found at large τ in Fig. 2 and is confirmed by our model (equation 21; dotted line in Fig. 9). Our prediction is offset from the measurement due to uncertainties in the modelling, but the slopes agree well.

Although polynomial fits using equation (18) warrant cubic terms in both cases, $\Delta F_\mathrm{rel}(\tau_i + \Delta\tau_i)$ is much straighter in the 'first pixel matched' case where also the ρ_i are altered (right-pointing triangles in Fig. 9; cf. Section 5.4.4). The reason is that the slopes of $\Delta F_\mathrm{rel}(\rho_i + \Delta\rho_i)$ and $\Delta F_\mathrm{rel}(\tau_i + \Delta\tau_i)$ have the same sign and do not partially cancel each other out, as is the case for $\Delta e_1(\rho_i + \Delta\rho_i)$ and $\Delta e_1(\tau_i + \Delta\tau_i)$. Again, equation (17) succeeds in predicting the measurements, despite offsets that are significant given the small uncertainties but small in terms of ΔF_rel in the uncorrected images.

Using the cubic fits, we find the following wide tolerance ranges (equation 19): $\Delta\tau^\mathrm{tol}_{3,\mathrm{min}}/\tau_3 = 15.7 \pm 0.2$ per cent and $\Delta\tau^\mathrm{tol}_{3,\mathrm{max}}/\tau_3 = 23.2^{+1.0}_{-0.9}$ per cent. In the 'first pixel matched' case, the intervals are considerably tighter, due to the contribution from the change in densities, with $\Delta\tau^\mathrm{tol}_{i,\mathrm{min}}/\tau_i = 2.625 \pm 0.007$ per cent and $\Delta\tau^\mathrm{tol}_{i,\mathrm{max}}/\tau_i = 2.630 \pm 0.007$ per cent. Again, the strictest constraints come from the ellipticity component Δe_1.

6 DISCUSSION

6.1 Limits of the predictive model

We measured tolerance ranges for changes in the ρ_i and τ_i given the *Euclid* VIS requirements, and presented a model (equation 17) capable of predicting these results based on the $\Delta\eta(\tau)$ curves (e.g. $\Delta e_1(\tau)$, Fig. 2), which are less expensive to obtain in terms of CPU time. However, as can be seen in particular in Fig. 7, there is a mismatch between predictions and measurements for τ_3, the most common baseline model trap species. As discussed in Section 5.4.4, this is caused by the finite sampling and the empirical nature of equation (14). There is ongoing work on improving our $\Delta\eta(\tau)$ models (Fig. 2).

Unfortunately, $f(\tau)$ and $f^\mathrm{resid}(\tau)$ will likely depend non-trivially on the source profile. Moreover, equation (17), if applied to ellipticity, treats it as additive. Where this approximation breaks down, i.e. when values that are not $\ll 1$ are involved, the correct additional formula (e.g. Schneider 2006) must be used. This applies to CTI-induced ellipticity as well as to large intrinsic or shear components.

We tested that the dependence on β (Fig. 4) can be included in the model as well, yielding

$$\Delta f^\mathrm{Pr}(\beta, \rho_i, \tau_i) = \sum_i \rho_i f^\mathrm{resid}(\tau_i) + [f(\beta + \Delta\beta) - f(\beta)] \times \sum_i [\rho_i f(\tau_i) - (\rho_i + \Delta\rho_i) f(\tau_i + \Delta\tau_i)] \,. \quad (22)$$

6.2 Applicability

Our findings pertain specifically to CTI correction employing the Massey et al. (2014) iterative correction scheme, the current nominal procedure for *Euclid* VIS. Other algorithms for the removal of CTI trailing exist that might not be susceptible in the same way to readout noise. Prod'homme et al. (2012), investigating the full-forward approach designed for *Gaia*, did not observe a readout noise floor similar to the one we found. The same might hold for including CTI correction in a forward-modelling shear measurement pipeline (e.g. Miller et al. 2013). However, the *Gaia* method has not been applied yet to actual observational data, and the method of Massey et al. (2014) is the most accurate method for the CTI correction of real data today.

We remind the reader that our results on the zero-points upon correcting with the correct model (Fig. 4) are dependent on the specifics of the small and faint galaxies we simulated. Further tests will determine if the large bias in R^2 persists under more realistic scenarios.

The narrow tolerances of $\Delta\rho/\rho = 0.11$ per cent and $\Delta\tau/\tau = 0.17$ per cent for the density of the slow traps species might look daunting, but fortunately, due to the discernible trails caused by these traps, it is also the easiest species of which to determine the properties. Conversely, the $\Delta\rho/\rho = 3$ per cent and $\Delta\tau/\tau = 8$ per cent for the fast traps are much larger, but constraints on these traps will be harder to achieve from laboratory and in-flight

calibration data. The 'first pixel matched' case that takes into account how trap parameters are determined from CTI trails relaxes the tolerances from ellipticity, given our particular baseline trap mix. It also tightens the (much broader) photometry tolerances. We notice that, while trap parameters are degenerate and Section 5.4.4 marks a first attempt to disentangle these parameters, each (degenerate) set of parameters can yield a viable CTI correction. Characterizing the true trap species, however, is crucial with respect to device physics applications.

Source profile dependence of the CTI-induced flux bias $\Delta F_{\rm rel}$ will lead to a sample of realistic sources (i.e. with a distribution of source profiles) showing a range in $\Delta F_{\rm rel}$ at any given readout noise level. Thus, the uncertainty in $\Delta F_{\rm rel}$ will be larger than the 10^{-4} we measured for our broad-winged, but homogeneous images in Section 5.5.1. Tailored simulations that model the VIS photometric calibration pipeline will be necessary to assess the role of the variable CTI-induced flux bias in *Euclid*'s photometric error budget. This exceeds the scope of this paper, which focuses on image morphology.

7 CONCLUSIONS AND OUTLOOK

The goal was to bridge the divide between engineering measurements of CTI and its degradation of scientific measurements of measured galaxy surface brightness moments. We have developed a very fast algorithm to model CTI in irradiated e2v Technologies CCD273 devices, reproducing laboratory measurements performed at ESTEC. We take a worst-case approach and simulate the faintest galaxies to be studied by *Euclid*, with a broad-winged exponential profile, at the end of the mission and furthest away from the readout register. Our analysis is hindered by the divergent surface brightness moments of the Marsaglia–Tin distribution that the ellipticity components follow. We alleviate this problem by means of a Taylor expansion around the mean of the denominator, yielding an accuracy of $\sigma e_\alpha \approx 10^{-4}$ by averaging over 10^7 simulated images. We advocate that *Euclid* requirements be re-defined in a way that avoids ratios of noisy quantities.

Our detailed study of the trapping process has confirmed that not all traps are equally bad for shape measurement (Rhodes et al. 2010). Traps with release time-scales of a few clocking cycles cause the largest spurious ellipticity, while all traps with longer τ_i yield the strongest flux bias.

The impact of uncertainties in the trap densities ρ_i and time-scales τ_i on CTI effects can be predicted to a satisfactory accuracy by a model that is linear in the ρ_i and additive in the effects of different trap species. For future applications, this will allow us to reduce the simulational effort in CTI forecasts, calculating the effect of trap pixels from single-species data.

Informed by laboratory data of the irradiated CCD273, we have adopted a baseline trap model for *Euclid* VIS forecasts. We corrected images with a trap model $\boldsymbol{M} + \delta\boldsymbol{M}$ offset from the model $\boldsymbol{M}$ used for applying CTI. Thus, we derived tolerance ranges for the uncertainties in the trap parameters, given *Euclid* requirements, positing that the required level of correction will be achieved. We conclude the following.

(1) In the absence of readout noise, perfect CTI correction in terms of ellipticity and flux can be achieved.

(2) Given the nominal rms readout noise of 4.5 electrons, we measure $Z_{e_1} = \Delta e_1 = -1.18 \times 10^{-3}$ after CTI correction. This still exceeds the *Euclid* requirement of $|\Delta e_1| < 1.1 \times 10^{-4}$. The requirement may still be met on the actual ensemble of galaxies *Euclid* will measure, since we consider only the smallest galaxies of S/N = 11. Likewise, in S/N = 200 stars, we measure a size bias of 1.12×10^{-3}, exceeding the requirement of $|\Delta R^2/R^2_{\rm true}| < 4 \times 10^{-4}$.

(3) The spurious ellipticity Δe_1 sensitively depends on the correct well fill power β, which we need to constrain to an accuracy of $\Delta\beta_{\rm tol} = (6.31 \pm 0.07) \times 10^{-5}$ to meet requirements. This assumes calibration by a single, bright charge injection line. The narrowest tolerance intervals are found for the dominant slow trap species in our baseline mix: $\Delta\rho_{\rm tol}/\rho_0 = (\pm 0.0272 \pm 0.0005)$ per cent and $\Delta\tau_{\rm tol}/\tau_0 = (\pm 0.0400 \pm 0.004)$ per cent.

(4) Given the nominal rms readout noise, we measure a flux bias $Z_{\rm F} = \Delta F_{\rm rel} = (-1.980 \pm 0.012)$ per cent after CTI correction, outside the required $|\Delta F_{\rm rel}| < 0.7$ per cent for the photometric uncertainty. However, the relevant quantity will be the *uncertainty of this bias*, which for realistic sources depends on their source profile. Further study is necessary here, as well as for the impact of CTI on photometric non-linearity.

The final correction will only be as good as on-orbit characterization of physical parameters such as trap locations, density, and release time. The next steps building on this study should include: (1) researching and testing novel algorithms mitigating the effects of readout noise as part of the CTI correction; (2) characterizing the effect of realistic source profile distributions in terms of the photometric and non-linearity requirements; and (3) translating the tolerances in trap model parameters into recommendations of calibration measurements and their analysis, based on modelling the characterization of trap species.

Plans for *Euclid* VIS calibration have already been updated to include charge injection at multiple levels such that β does not need to be extrapolated from bright charge injection lines to faint galaxies. We will continue to liaise between engineers and scientists to determine how accurately it will be necessary to measure these physical parameters. The VIS readout electronics will be capable of several new in-orbit calibration modes such as trap pumping (Murray et al. 2012) that are not possible with *HST*, and our calculations will advise what will be required, and how frequently they need to be performed, in order to adequately characterize the instrument for scientific success.

ACKNOWLEDGEMENTS

This work used the DiRAC Data Centric system at Durham University, operated by the Institute for Computational Cosmology on behalf of the STFC DiRAC HPC Facility (www.dirac.ac.uk). This equipment was funded by BIS National E-infrastructure capital grant ST/K00042X/1, STFC capital grants ST/H008519/1 and ST/K00087X/1, and STFC DiRAC Operations grant ST/K003267/1 and Durham University. DiRAC is part of the National E-Infrastructure.

HI thanks Lydia Heck and Alan Lotts for friendly and helpful system administration. HI acknowledges support through European Research Council grant MIRG-CT-208994. RM and HI are supported by the Science and Technology Facilities Council (grant numbers ST/H005234/1 and ST/N001494/1) and the Leverhulme Trust (grant number PLP-2011-003). JR was supported by JPL, run under a contract for NASA by Caltech. OC and OM acknowledge support from the German Federal Ministry for Economic Affairs and Energy (BMWi) provided via DLR under project no. 50QE1103.

The authors thank Henk Hoekstra, Peter Schneider, Yannick Mellier, Tom Kitching, Reiko Nakajima, Massimo Viola, and the

members of *Euclid* CCD Working group, *Euclid* OU-VIS, and OU-SHE groups for comments on the text and useful discussions.

REFERENCES

Anderson J., Bedin L. R., 2010, PASP, 122, 1035
Bertin E., Arnouts S., 1996, A&AS, 117, 393
Bristow P., 2003, preprint (astro-ph/0310714)
Casella G., Berger R. L., 2002, Statistical Inference, 2nd edn. Duxbury, Pacific Grove
Cropper M. et al., 2013, MNRAS, 431, 3103
Cropper M. et al., 2014, Proc. SPIE, 9143, 91430J
Endicott J. et al., 2012, Proc. SPIE, 8453, 845304
Gow J. P. D., Murray N. J., Hall D. J., Clarke A. S., Burt D., Endicott J., Holland A. D., 2012, Proc. SPIE, 8453, 845316
Kacprzak T., Zuntz J., Rowe B., Bridle S., Refregier A., Amara A., Voigt L., Hirsch M., 2012, MNRAS, 427, 2711
Kaiser N., Squires G., Broadhurst T., 1995, ApJ, 449, 460
Kitching T. D. et al., 2012, MNRAS, 423, 3163
Kohley R. et al., 2014, Proc. SPIE, 9154, 915406
Laureijs R. et al., 2011, preprint (arXiv:1110.3193)
Leauthaud A. et al., 2007, ApJS, 172, 219
Lindegren L. et al., 2008, in Jin W. J., Platais I., Perryman M. A. C., eds, Proc. IAU Symp. 248, A Giant Step: From Milli- to Micro-Arcsecond Astrometry. Cambridge Univ. Press, Cambridge, p. 217
Markwardt C. B., 2009, in Bohlender D. A., Durand D., Dowler P., eds, ASP Conf. Ser. Vol. 411, Astronomical Data Analysis Software and Systems XVIII. Astron. Soc. Pac., San Francisco, p. 251
Marsaglia G., 1965, J. Am. Stat. Assoc., 60, 193
Marsaglia G., 2006, J. Stat. Softw., 16, 1
Massey R., 2010, MNRAS, 409, L109
Massey R., Stoughton C., Leauthaud A., Rhodes J., Koekemoer A., Ellis R., Shaghoulian E., 2010, MNRAS, 401, 371
Massey R. et al., 2013, MNRAS, 429, 661
Massey R. et al., 2014, MNRAS, 439, 887
Melchior P., Viola M., 2012, MNRAS, 424, 2757
Miller L. et al., 2013, MNRAS, 429, 2858
Moré J. J., 1978, in Watson G., ed., Lecture Notes in Mathematics, Vol. 630, Numerical Analysis. Springer-Verlag, Berlin, p. 105
Murray N. J., Holland A. D., Gow J. P. D., Hall D. J., Tutt J. H., Burt D., Endicott J., 2012, Proc. SPIE, 8453, 845317
Prod'homme T., Holl B., Lindegren L., Brown A. G. A., 2012, MNRAS, 419, 2995
Prod'homme T., Verhoeve P., Kohley R., Short A., Boudin N., 2014, Proc. SPIE, 9154, 915409
Refregier A., Amara A., Kitching T. D., Rassat A., Scaramella R., Weller J., Euclid Imaging Consortium 2010, preprint (arXiv:1001.0061)
Refregier A., Kacprzak T., Amara A., Bridle S., Rowe B., 2012, MNRAS, 425, 1951
Rhodes J., Refregier A., Groth E. J., 2001, ApJ, 552, L85
Rhodes J., Leauthaud A., Stoughton C., Massey R., Dawson K., Kolbe W., Roe N., 2010, PASP, 122, 439
Schneider P., 2006, in Meylan G., Jetzer P., North P., eds, Saas-Fee Advanced Courses, Vol. 33, Gravitational Lensing: Strong, Weak and Micro. Springer, Berlin, p. 269
Seabroke G., Holland A., Cropper M., 2008, Proc. SPIE, 7021, 70211P
Short A., Crowley C., de Bruijne J. H. J., Prod'homme T., 2013, MNRAS, 430, 3078
Short A. D. et al., 2014, Proc. SPIE, 9154, 91540R
Smith L. J. et al., 2012, in Marvel K. B., ed., American Astronomical Society Meeting Abstracts, Vol. 219, p. 241.01
Stassinopoulos E. G., Raymond J. P., 1988, Proc. IEEE, 76, 1423
Tin M., 1965, J. Am. Stat. Assoc., 60, 294
Verhoeve P., Prod'homme T., Oosterbroek T., Boudin N., Duvet L., 2014, Proc. SPIE, 9154, 915416
Viola M., Kitching T. D., Joachimi B., 2014, MNRAS, 439, 1909

APPENDIX A: INFORMING THE BASELINE MODEL WITH LABORATORY DATA

A1 EPER/FPR data with irradiated CCD

In this appendix, we define a baseline CTI model for *Euclid* VIS. Our model is based upon laboratory tests of an irradiated e2v Technologies back-illuminated *Euclid* prototype CCD273, analysed at ESA/ESTEC (Prod'homme et al. 2014). The device was irradiated at ambient room temperature using 10.4 MeV protons, degraded from a 38.5 MeV primary proton beam at the Kernfysisch Versneller Instituut, Groningen, in 2013 April. Two different shielding masks were used (Prod'homme et al. 2014) resulting in the four quadrants of the CCD, called E, F, G, and H, and corresponding to the four output nodes, receiving different radiation doses. Each a half of two quadrants, called G and H, received a 10 MeV equivalent fluence of 4.8×10^9 protons cm^{-2}, representative of the predicted end-of-life (eol) proton fluence for *Euclid*. Half of the F quadrant was irradiated with a 10 MeV equivalent fluence of 2.4×10^9 protons cm^{-2}, the eol/2 fluence. Neither the E quadrant, the serial register of the H quadrant, nor the readout nodes were irradiated (Prod'homme et al. 2014; Verhoeve et al. 2014).

At the ESA Payload Technology Validation section CCD test bench located at ESTEC (Verhoeve et al. 2014), the irradiated CCD273 was characterized at the *Euclid* VIS nominal conditions of 153 K temperature and a 70 kHz readout frequency. While a serial clocking scheme with the same width for each register phase at each step was used, minimizing serial CTI, the nominal line/parallel transfer duration of 0.11 ms was not optimized.

As part of the characterization, a suite of EPER and FPR experiments were performed, at different flat-field signal levels. For the purpose of deriving a fiducial baseline model of the charge traps present in the CCD273, we focus on the parallel EPER (pEPER) and serial EPER (sEPER) data. To study the sEPER CTI, a flat-field image is taken, then the half opposite to the readout direction is dumped, and finally the frame is read out. This yields a flat-field with a sharp trailing edge in flat-field signal. Electrons captured from flat-field pixels are being released into signal-less pixels, resulting in a CTI trail. Our pEPER tests make use of the parallel overscan region, providing a similar signal edge.

Each measurement was performed repeatedly, in order to gather statistics: 45 times for the sEPER data at low signal and 20 times for the pEPER data. Raw trail profiles are extracted from the first 200 pixels following the signal edge, taking the arithmetic mean over the independent lines perpendicular to the direction (serial or parallel) of interest. The same is done in the overscan region, unexposed to light, and the pixel-by-pixel median of this reference is subtracted as background from the raw trails. In the same way as the reference, the median flat-field signal is determined, and also corrected for the overscan reference. Finally, the trail (flat-field signal) at zero flat-field exposure time is subtracted from the trails (flat-field signals) at exposure times >0.

Fig. A1 shows the resulting 'uncalibrated' trail profiles for the sEPER (upper panel) and pEPER (lower panel) measurements in the G quadrant (eol radiation dose), at a flat-field exposure time corresponding to an average of 1018 signal electrons per pixel. These are the upper solid lines with light grey shading denoting the propagated standard errors from the repeated experiments. Effects in the readout electronics mimic CTI. We correct for the electronic effect by subtracting the average trail in the unirradiated quadrants (E for pEPER, and E and H for sEPER). The resulting 'calibrated' trail profiles and their uncertainties are presented as the lower solid

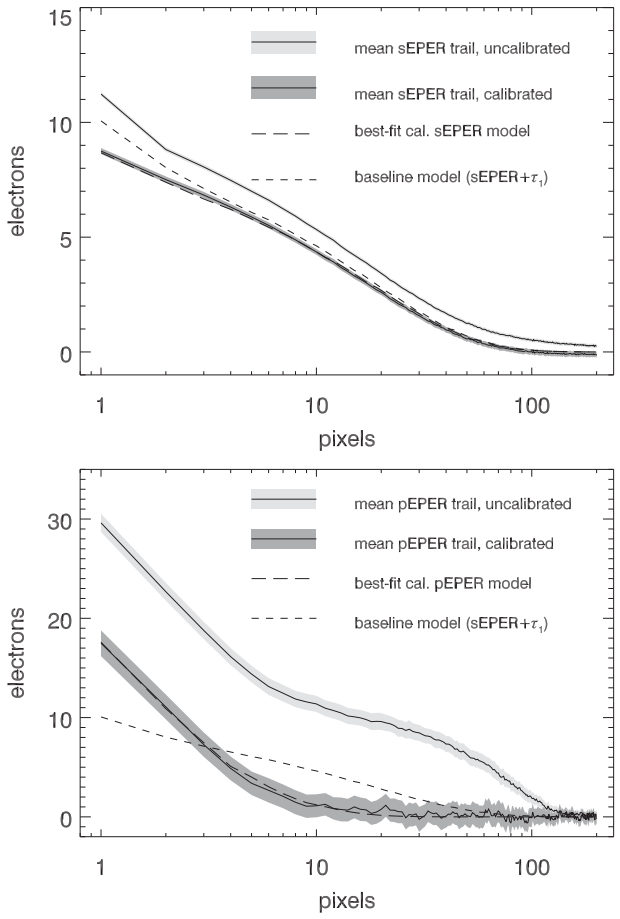

Figure A1. CCD273 EPER trails in the serial (upper plot) and parallel (lower plot) directions. Shown here are the G quadrant trails at an input signal of ∼1000 electrons. Solid lines within the light and dark grey shaded areas denote the average and its uncertainty of the profile before and after correction for electronic effects. The best-fitting model to the corrected trail is shown as a long-dashed line. For the purpose of illustration, the baseline trap model is shown in both plots as a short-dashed line. Building on the sEPER model, the baseline model includes fast traps that are seen in quadrant F.

lines and dark grey shadings in Fig. A1. The calibration makes a small correction to the sEPER trail which is dominated by slow traps, yielding a significant signal out to ∼60 pixels. In contrast, the electronic effect accounts for 1/3 of the uncalibrated pEPER trail even in the first pixel, and for all of it beyond the tenth. Thus, the S/N in the calibrated trail is much lower.

A2 The well fill power β

In a volume-driven CTI model, the cloud of photoelectrons in any given pixel is assumed to fill up a height within the silicon that increases as electrons are added (equation 12). The growth of the cloud volume is governed by the term $\left(\frac{n_e}{w}\right)^{\beta} \sum_i \rho_i$ in equation (12), with the full-well depth $w = 84\,700$ limiting the maximum number of electrons in a pixel. There is no supplementary buried channel in the CCD273, which for *HST*/ACS leads to the first ∼100 electrons effectively occupying zero volume (Massey et al. 2010).

We use measurements of the integrated EPER as a function of input signal to constrain the well fill power β of the trapping model. Our simulated galaxies are faint; so we restrict ourselves to the

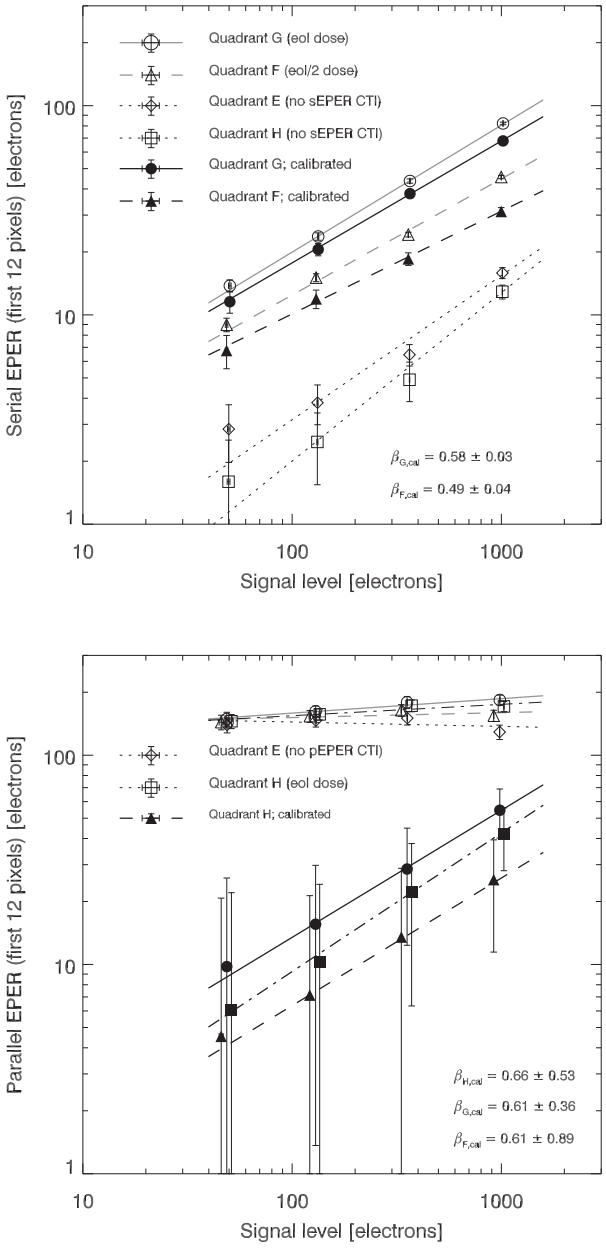

Figure A2. The well fill power β measured from the integrated EPER CTI as a function of input signal. The upper panel shows the results from the sEPER measurements, for which CTI is present in the F and G quadrants and can be corrected using the E and H quadrants. The lower panel shows the results from the pEPER measurements, for which CTI is present in the F, G, and H quadrants and can be corrected using the E quadrant. Open symbols denote the raw measurements, and filled symbols the calibrated measurements from which the fits for β are derived.

four lowest signal levels measured in the laboratory, with up to ∼1000 electrons. The input signal is measured as the average count difference between the flat-field and overscan regions, corrected for the CCD gain.

Fig. A2 shows the CTI trails from Fig. A1, integrated over the first 12 pixels. We checked that integrating over up to the full overscan region length of 200 pixels does not change the results drastically. In the sEPER data (upper panel of Fig. A2), the unirradiated quadrants E and H (open squares and diamonds) exhibit very small trail

integrals (caused by the readout electronics), one order of magnitude smaller than in the irradiated quadrants F and G (open circle and triangle). Hence, calibrating out the instrumental effect by subtracting the arithmetic average from the E and H quadrants yields only a small correction to the F and G trail integrals. To these calibrated sEPER measurements (filled circle and triangle), we fit linear relations in log–log space using the IDL `fitexy` routine and measure $\beta_{\mathrm{F,\,cal}} = 0.49 \pm 0.04$ and $\beta_{\mathrm{G,\,cal}} = 0.58 \pm 0.03$.

We repeat this procedure for the pEPER measurements where the unirradiated E quadrant shows a similar EPER integral as the irradiated F, G, and H quadrants (lower panel of Fig. A2). Thus, the pEPER and sEPER integrals may yield similar values as a function of signal, but for pEPER the low S/N $\ll 1$ causes large uncertainties. Consequently, β is not well constrained, with $\beta_{\mathrm{F,\,cal}} = 0.66 \pm 0.53$, $\beta_{\mathrm{G,\,cal}} = 0.61 \pm 0.36$, and $\beta_{\mathrm{H,\,cal}} = 0.61 \pm 0.89$, but they agree with the sEPER results.

In conclusion, we adopt a baseline well fill power of $\beta_0 = 0.58$ for our further tests, based on the precise sEPER result for the full radiation dose.

A3 From trail profiles to trap parameters

To constrain the trap release time-scales τ_i and trap densities ρ_i, we make use of the two signal levels of ∼360 electrons and ∼1000 electrons that bracket the number of electrons we expect to be found in a typical faint *Euclid* galaxy. These are the two highest data points in Fig. A2. We compare the average, measured, calibrated trails from the irradiated quadrants (examples for the G quadrant are presented in Fig. A1) and compare them to the output a one-dimensional version of our Massey et al. (2014) clocking routine produces given trap densities ρ_i and release time-scales τ_i, and under circumstances close to the laboratory data (i.e. a 200 pixel overscan region following a 2048 pixel flat-field column of 1018 signal electrons). The fitting is performed using the `MPFIT` implementation of the Levenberg–Marquardt algorithm for non-linear regression (Moré 1978; Markwardt 2009).

Fitting a sum of exponentials is remarkably sensitive to noise in the data because the parameters (τ_i and ρ_i) we are probing are intrinsically correlated. We assess the robustness of our results by repeating the fit not only for the two (three) irradiated sEPER (pEPER) quadrants at two signal levels, but for a wide range of trail lengths (60 to 150) we consider, and with and without adding a constant term.

Table A1. The same as Table 2, but for the best-fitting models shown in Fig. A1. The baseline well fill power is $\beta_0 = 0.58$.

Best-fitting sEPER model	$i = 1$	$i = 2$	$i = 3$
Trap density ρ_i [pixel^{-1}]	0.01	0.03	0.90
Release time-scale τ_i [pixel]	0.8	3.5	20.0
Release time-scale τ_i [ms]	186	814	4649
Best-fitting pEPER model	$i = 1$	$i = 2$	$i = 3$
Trap density ρ_i [pixel^{-1}]	0.13	0.25	–
Release time-scale τ_i [pixel]	1.25	4.4	–
Release time-scale τ_i [μs]	142	499	–

There are several possible trap species as defined by their τ_i that show up in our data set. We rule out those of very low densities and consider the frequent 'species' whose time-scales are within a few per cent of each other as one. Still, this leaves us with more than one contesting family of trap species that yet give similar trails in some of the quadrant/signal combinations. Because, at this stage, our goal is to derive *a plausible baseline model* rather than pinpointing the correct trap species, we filter for the most common τ_i and give precedence to the higher-S/N data (sEPER, eol dose, 1000 signal electrons). The resulting best-fitting models are shown in Table A1 and Fig. A1. The actual baseline model (Table 2; short-dashed line in Fig. A1) includes additional fast traps seen in the lower-S/N data. We raise the density from 0.94 traps per pixel to a mnemonic total of 1 trap per pixel at eol dose. More refined methods will be used to determine the trap species in a more detailed analysis of irradiated CCD273 data.

Because only 464 pixels of the serial register in the test device were irradiated, the effective density of charge traps an electron clocked through it experiences is smaller by a factor of 464/2051 than the actual trap density corresponding to the eol radiation dose that was applied. We correct for this by quoting results that have been scaled up by a factor of $2051/(464 \times 0.94) \approx 4.155$.

A4 Example CTI trails

Fig. A3 shows, for the largest deviations from the baseline trap model we consider, their effect on the shape of the CTI trails. Using our CTI model, we simulated the trail caused by a single pixel containing a signal of ∼1000 electrons, comparable to a hot pixel in actual CCD data.

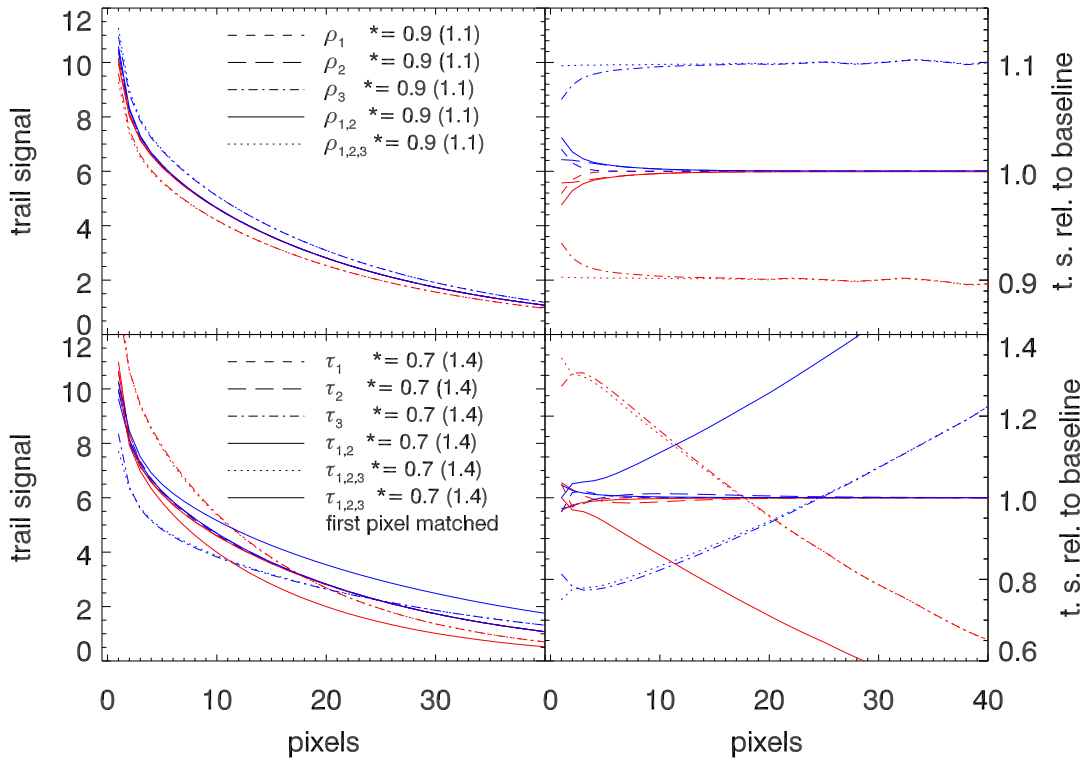

Figure A3. Trail profiles corresponding to our trap models. Upper-left panel: trails for models in which the densities ρ_i are modified by a factor of 0.9 (red) or 1.1 (blue). This is applied to the fast traps ρ_1 (dashed lines); the medium traps ρ_2 (long-dashed lines); the slow traps ρ_3 (dot–dashed lines); ρ_1 and ρ_2 (triple dot–dashed lines); and all traps (dotted lines). Upper-right panel: the same, but relative to the baseline model. Lower-left panel: trails for trap models in which the release time-scales τ_i are modified by a factor of 0.7 (red) or 1.4 (blue). The line code is the same as above. Solid lines show models in which not only all the τ_i are changed, but also the ρ_i adjusted such that the first pixel matches the baseline trail profile (Section 5.4.4). Lower-right panel: the same, but relative to the baseline model.

This paper has been typeset from a TEX/LATEX file prepared by the author.